DEPARTMENT OF MECHANICAL ENGINEERING AND MECHANICS
SCHOOL OF ENGINEERING
OLD DOMINION UNIVERSITY
NORFOLK, VIRGINIA

A NUMERICAL SIMULATION OF TRANSITION IN PLANE CHANNEL FLOW

By

G. Goglia, Principal Investigator

and

S. Biringen, Co-Principal Investigator

Final Report
For the period October 1, 1981 to September 30, 1982

Prepared for the
National Aeronautics and Space Administration
Langley Research Center
Hampton, Virginia

Under
Research Grant NAG1-278
W.D. Harvey, Technical Monitor

(NASA-CR-165322) A NUMERICAL SIMULATION OF TRANSITION IN PLANE CHANNEL FLOW Final Report, 1 Oct. 1981 - 30 Sep. 1982 (Old Dominion Univ., Norfolk, Va.) 49 p
HC A03/MF A01 CSCL 20D G3/34

N82-32636

Unclas
26951

August 1982

TABLE OF CONTENTS

	Page
SUMMARY	1
1. INTRODUCTION	1
2. THE CALCULATION PROCEDURE	4
3. RESULTS AND DISCUSSION	9
REFERENCES	19

LIST OF FIGURES

Figure		
1	Time-history of maximum disturbance amplitudes. (a) two-dimensional primary; (b) three-dimensional primary; (c) two-dimensional harmonic	21
2	Plots of plane-averaged mean velocity profiles. (a) T = 0; (b) T = 42; (c) T = 50	22
3	Plots of instantaneous velocity profiles at $x_1 = 3\pi/2$, $x_3 = \pi/2$. (a) T = 12; (b) T = 42; (c) T = 50	23
4	Plots of plane-averaged mean velocity in wall units; ○, T = 42; △, T = 50; ——, law-of-the-wall; ●--, experiments of Nishioka et al. (1981) at the five-spike stage	24
5	Plots of plane-averaged fluctuating intensities. (a) T = 0; (b) T = 22; (c) T = 42; ●--, experiments of Nishioka et al. (1981) at the five-spike stage	25
6	Spanwise variations of u_1 at T = 42. (a) $x_2 = 0.029$; (b) $x_2 = 0.099$; (c) $x_2 = 0.256$	26
7	Spanwise variations of u_3 at T = 42. (a) $x_2 = 0.029$; (b) $x_2 = 0.099$; (c) $x_2 = 0.256$	27
8	Contour plots of $\frac{\partial u_1}{\partial x_2}$ at T = 0 in the x_1, x_2 plane. Contours from -0.3 to 7.2	28

TABLE OF CONTENTS

	Page
SUMMARY	1
1. INTRODUCTION	1
2. THE CALCULATION PROCEDURE	4
3. RESULTS AND DISCUSSION	9
REFERENCES	19

LIST OF FIGURES

Figure		
1	Time-history of maximum disturbance amplitudes. (a) two-dimensional primary; (b) three-dimensional primary; (c) two-dimensional harmonic	21
2	Plots of plane-averaged mean velocity profiles. (a) T = 0; (b) T = 42; (c) T = 50	22
3	Plots of instantaneous velocity profiles at $x_1 = 3\pi/2$, $x_3 = \pi/2$. (a) T = 12; (b) T = 42; (c) T = 50	23
4	Plots of plane-averaged mean velocity in wall units; o, T = 42; Δ, T = 50; ——, law-of-the-wall; ●--, experiments of Nishioka et al. (1981) at the five-spike stage	24
5	Plots of plane-averaged fluctuating intensities. (a) T = 0; (b) T = 22; (c) T = 42; ●--, experiments of Nishioka et al. (1981) at the five-spike stage	25
6	Spanwise variations of u_1 at T = 42. (a) $x_2 = 0.029$; (b) $x_2 = 0.099$; (c) $x_2 = 0.256$	26
7	Spanwise variations of u_3 at T = 42. (a) $x_2 = 0.029$; (b) $x_2 = 0.099$; (c) $x_2 = 0.256$	27
8	Contour plots of $\frac{\partial u_1}{\partial x_2}$ at T = 0 in the x_1, x_2 plane. Contours from -0.3 to 7.2	28

LIST OF FIGURES - CONTINUED

Figure		Page
9	Contour plots of $\frac{\partial u_1}{\partial x_2}$. (a) three-spike stage, figure from Nishioka et al. (1981); (b) computations at T = 42 in the x_1,x_2 plane; contours from -1.2 to 6.0.....	29
10	Contour plots of $\frac{\partial u_1}{\partial x_2}$. (a) three-spike stage, figure from Nishioka et al. (1981); (b) computations at T = 22 in the x_1,x_2 plane; contours from -0.3 to 5.1.....	30
11	Contour plots of $\frac{\partial u_1}{\partial x_2}$. (a) five-spike stage, figure 6 from Nishioka et al. (1981); (b) computations at T = 42 in the x_1,x_2 plane; contours from -0.6 to 9.0.....	31
12	Contour plots of $\frac{\partial u_1}{\partial x_2}$, at T = 50 in the x_1,x_2 plane; contours from -0.6 to 9.0.....	32
13	Contour plots of ω_x in the x_2, x_3 plane at T = 0; contours from -0.03 to 0.03, labels scaled by 10000.....	33
14	Contour plots of ω_x in the x_2, x_3 plane at T = 12; contours from -1.6 to 1.6.....	34
15	Contour plots of ω_x in the x_2, x_3 plane at T = 22; contours from -4.8 to 4.8.....	35
16	Contour plots of ω_x in the x_2, x_3 plane at T = 42; contours from -6.4 to 6.4.....	36
17	Contour plots of ω_x in the x_2, x_3 plane at T = 50; contours from -5.4 to 5.4.....	37
18	Contour plots of ω_x in the x_2, x_3 plane at T = 50; contours from -5.6 to 5.6.....	38
19	Contour plots of u_1 in the x_1, x_2 plane at T = 22; contours from -0. to 0.96.....	39
20	Contour plots of u_2 in the x_1, x_2 plane at T = 22; contours from -0.081 to 0.072 labels scaled by 1000.....	40
21	Contour plots of u_2 in the x_1, x_2 plane at T = 42; contours from -0.22 to 0.20.....	41

LIST OF FIGURES - CONCLUDED

Figure		Page
22	Contour plots of u_2 in the x_2, x_3 plane at T = 42 in the vicinity of the lower wall; contours from -0.135 to 0.135.....	42
23	Contour plots of u_2 in the x_2, x_3 plane at T = 50 in the vicinity of the lower wall; contours from -0.135 to 0.135.....	43

A NUMERICAL SIMULATION OF TRANSITION IN PLANE CHANNEL FLOW

By

G. Goglia[1] and Sedat Biringen[2]

SUMMARY

This paper involves a numerical simulation of the final stages of transition to turbulence in plane channel flow at a Reynolds number of 7500. Three-dimensional, incompressible Navier-Stokes equations are numerically integrated to obtain the time-evolution of two- and three-dimensional finite-amplitude disturbances. Computations are performed on the CYBER-203 vector processor for a 32×33×32 grid. Solutions indicate the existence of structures similar to those observed in the laboratory and which are characteristic of various stages of transition that lead to final breakdown. Details of the resulting flow field after breakdown indicate the evolution of streak-like formations found in turbulent flows. Although the flow field does approach a steady-state (turbulent channel flow), implementation of subgrid-scale terms are necessary to obtain proper turbulent statistics.

1. INTRODUCTION

Recent experiments by Nishioka, Asia & Iida (1981) have shown that transition to turbulence in a plane channel flow follows a sequence of events similar to that observed by Klebanoff, Tidstrom & Sargent (1962) in the boundary-layer transition. In this work, a direct numerical integration of the Navier-Stokes equations is performed in an attempt to simulate these events in plane channel flow, during the later stages of transition.

In their experiments, Nishioka et al. (1981) used a vibrating ribbon technique to generate two-dimensional disturbances fixed at 72 Hz. To

[1] Eminent Professor/Chairman, Department of Mechanical Engineering and Mechanics, Old Dominion University, Norfolk, Virginia.

[2] Research Associate Professor, Department of Mechanical Engineering and Mechanics, Old Dominion University, Norfolk, Virginia.

excite the fully developed flow in a channel with a 27.4 aspect ratio. They measured the streamwise mean and fluctuating velocities, U_1 and u_1', respectively, at a fixed streamwise location at a subcritical (linearly stable) Reynolds number, Re = 5000 and simulated the various stages of transition by varying the disturbance amplitude. Their observations show that subcritical instability takes place at a threshold amplitude of $(u_1')_{max}/U_o = 0.01$, where U_o is the mean velocity at the channel centerline. The evolution of this instability is evidenced by the intensification of the spanwise variation of the wavefront which develops into a peak-valley structure. Nishioka et al. (1981) observed that flow development follows then a trend which is similar to transition in the boundary-layer (Klebanoff et al. 1962, Kovasznay, Komoda & Vasudeva 1962): local shear layers are formed away from the wall at spanwise peak positions ($u_1'/U_o = 0.11$). In rapid succession, two-, three-, five- and multi-spike stages are observed with increasing amplitude of the primary disturbance. Nishioka et al. (1981) present evidence that in the final stages of transition, the flow starts to develop structures very similar to those found in fully developed wall turbulence. During this stage, the flow field is characterized by the development of a viscous sublayer, occurrence of the typical "streaks" close to the wall and the formation of horseshoe vortices sometimes referred to as the building blocks of wall turbulence (Theodorsen 1954). The present work attempts to simulate this sequence of events.

Direct numerical integrations of the Navier-Stokes equations for the simulation of channel-flow transition has been the subject of some previous investigations. George & Hellums (1972) and Fasel, Bestek & Schefenacker (1977) used the two-dimensional Navier-Stokes equations to investigate the stability of channel flow to two-dimensional finite-amplitude disturbances. George & Hellum (1972) studied the relationship between critical amplitude and Reynolds number and found a minimum Reynolds number, Re = 3500, below which their predictions remained stable. This is contrary to experimental evidence (e.g., Kao & Park 1970) which indicates instability of plane channel flow to finite-amplitude disturbances at Reynolds number as low as 1000. Fasel et al. (1977) investigated the effects of disturbance amplitude on transition at subcritical and supercritical Reynolds numbers. They found

that increasing amplitude (u_1'/U_o = 0.06) of two-dimensional disturbances can drive plane channel flow to instability at a subcritical Reynolds number, Re = 5000. Although some insight into finite-amplitude instability of two-dimensional disturbances can be obtained from such calculations, a proper simulation of the transition process requires the use of the three-dimensional Navier-Stokes equations. Once the process extends into the nonlinear regime, transition becomes increasingly three-dimensional so that for a relistic (physically plausible) representation of flow breakdown, spanwise variations of the flow field variables must be accounted for. It is also well known that creation of vorticity through vortex stretching, an essential ingredient of transition, can take place only in a three-dimensional flow field. Hence, numerical solutions of the two-dimensional Navier-Stokes equations cannot represent energy transfer down the wave-number spectrum, which is the basic mechanisms of laminar flow transition to turbulence and the result of the vortex stretching mechanism.

Effects of three dimensionality on transition have first been documented in detail by Klebanoff et al. (1962). Accordingly, three-dimensionality manifests itself mainly in the spanwise velocity variations resulting in the production of streamwise vorticity which, in turn, interacts with the spanwise vorticity and drives the flow to breakdown. Orszag & Kells (1980) and Patera & Orszag (1981) have expanded on this idea to study the susceptibility of plane channel flow to three-dimensional disturbances by numerically integrating the three-dimensional Navier-Stokes equations. Their computations at subcritical Reynolds numbers revealed some interesting aspects of subcritical transition. They found that initial disturbances, which are finite-amplitude two-dimensional Orr-Sommerfeld eigensolutions, decay slowly and, as expected, rate of decay increases with decreasing Reynolds number. They also found that the addition of three-dimensional, finite-amplitude disturbances promote rapid instability at Reynolds numbers as low as 1000, which is in good agreement with the experiments of Kao & Park (1970). Their results suggest a similar tendency of the flow to instability even for small-amplitude, three-dimensional disturbances. They conclude that the mechanism that drives plane channel flow to instability is the interaction of two-dimensional and three-dimensional disturbances, supporting the idea

that three-dimensionality is central to transition in plane channel flow. In a more recent work, Kleiser (1982) incorporated r spectral method to solve the three-dimensional Navier-Stokes equations starting with weakly three-dimensional initial conditions. Comparisons of his results with the experiments of Nishioka, Asai & Iida (1980) up to the first spike stage are favorable even from a quantitative point of view supporting the idea that direct numerical simulations can be used as a mean of investigating the nonlinear transition process.

It is apparent that the complete simulation of transition requires the inclusion of non-linearity and three-dimensionality as the fundamental characteristics of the flow field. These effects are of primary importance in the present work wherein the main emphasis is on the final stages of transition. Hence, for an accurate representation of the underlying physical phenomena that take place during this stage of transition, the present simulation has been done by using the full three-dimensional, time-dependent Navier-Stokes equations. In order to drive the flow to instability and transition rapidly, calculations are performed at a linearly unstable Reynolds number (Re = 7500), with finite-amplitude two- and three-dimensional eigensolutions of the Orr-Sommerfeld equation used as the initial conditions. No attempt is made in this work to investigate the effects of different initial conditions or of Reynolds numbers. In section 2, the numerical methods used in the present study are briefly discussed. In section 3, results of calculations are presented and compared with the experiments of Nishioka et al. (1981). Finally, section 4 contains a summary of results and some concluding remarks.

2. THE CALCULATION PROCEDURE

The calculation procedure is based on the incompressible Navier-Stokes equations in primitive-variable form,

$$\frac{\partial u_i}{\partial t} + u_\ell \frac{\partial u_i}{\partial x_\ell} = -\frac{1}{\rho}\frac{\partial p'}{\partial x_i} + \nu \frac{\partial^2 u_i}{\partial x_\ell \partial x_\ell} \qquad (1)$$

and the continuity equation,

$$\frac{\partial u_i}{\partial x_i} = 0 \tag{2}$$

where u_i are the velocities along the x_i directions, ρ is the density, ν is the kinematic viscosity and p' is the total hydrostatic pressure. The equations are non-dimensionalized by the mean centerline velocity U_o and the channel half-width, h. The flow is assumed to be driven by a constant mean pressure gradient 2/Re, where Re is the Reynolds number given by $U_o h/\nu$. Also, the convective terms are put into a form which prevents occurrence of nonlinear instability in the numerical solution procedure by ensuring conservation of momentum and energy (Mansour, Ferziger, & Reynolds 1978). The final form of the Navier-Stokes equations reads,

$$\frac{\partial u_i}{\partial t} + u_\ell \left(\frac{\partial u_i}{\partial x_\ell} - \frac{\partial u_\ell}{\partial x_i} \right) = - \frac{\partial p}{\partial x_i} + \frac{2}{Re} \delta_{i1} + \frac{1}{Re} \frac{\partial^2 u_i}{\partial x_\ell \partial x_\ell} \tag{3}$$

where $P = p'/\rho + \frac{1}{2} u_\ell u_\ell$ is the pressure head and $\delta_{i\ell}$ is the Kronecker delta.

The flow is assumed to be periodic in the streamwise x_1 and the spanwise x_3 directions along which the flow field variables can be expanded in terms of Fourier series. This enables the use of the pseudo-spectral method (Orszag 1972) to calculate the spatial derivatives along x_1 and x_3 by use of discrete Fourier transforms. Considering transforms in the x_1-direction, along which there are N_1 equally spaced mesh points, the velocity component u_1 can be written as

$$u_1(x_1) = \sum_{n_1 = -N/2}^{N/2-1} \hat{u}_1(k_1) e^{ik_1 x_1} \tag{4}$$

where $x_1 = m\Delta x_1$, $m = 0,1,\ldots,N-1$ and $k_1 = 2\pi n_1 \Delta x_1$. Accordingly, the Fourier transform of u_1 is

$$\hat{u}_1(k_1) = \frac{1}{N_1} \sum_{m=0}^{N_1-1} u_1(x_1) e^{-ik_1 x_1} \tag{5}$$

The spatial derivative of u_1 along x_1 can now be written as

$$\frac{\partial u_1(x_1)}{\partial x_1} = \sum_{n_1=-N_1/2}^{N_1/2-1} ik_1 u_1(k_1) e^{ik_1 x_1} \qquad (6)$$

The derivative can be computed by forming the Fourier transform of $u_1(x_1)$, multiplying the result by ik_1 and computing the inverse transform. For periodic functions, the pseudo-spectral method provides a means by which the spatial derivatives are evaluated with maximum accuracy for a given number of grid points. Along the x_2-direction, a mesh stretching that concentrates grid points close to the solid walls is employed. The resulting mesh enables the resolution of the sublayer that is formed during transition for $y+ < 2$, where y^+ is the coordinate along x_2, in wall units. Spatial derivatives along x_2 are evaluated by a second-order finite-difference scheme on this non-uniform mesh.

The governing equations were numerically integrated by the semi-implicit method of Moin, Reynolds & Ferziger (1978). This procedure employs the explicit Adams-Bashforth method for the convective terms and the implicit Crank-Nicholson method for pressure and for the viscous diffusion terms. In order to start the two time-level Adams-Bashforth method, the Euler-implicit method is used at the first time step.

Once the governing equations are discretized in time, a two-dimensional Fourier transform along the periodic directions x_1 and x_3 transforms the equations into the k_1-k_3 wave-number space. The transformed equations are written below in block-tridiagonal form for inversion along x_2

$$\underline{A}\, \underset{\sim}{F}_{j+1}^{n+1} + \underline{B}\, \underset{\sim}{F}_{j}^{n+1} + \underline{C}\, \underset{\sim}{F}_{j-1}^{n+1} = \underset{\sim}{R}_{j}^{n} \qquad (7)$$

In (7), $\underline{A}$, $\underline{B}$, and $\underline{C}$ are coefficient matrices, $\underset{\sim}{F}_j^{n+1}$ is the solution vector at the advanced time level, n+1, and at the x_2-directional node, j; $\underset{\sim}{R}_j^n$ is the right-hand side vector that contains the convective, diffusive and pressure terms at the previous time levels. These are given as

$$\underset{\sim}{F} = \begin{bmatrix} \hat{u}_1 \\ \hat{u}_2 \\ \hat{u}_3 \\ P \end{bmatrix} \quad \underline{A} = \begin{bmatrix} C2_j & 0 & 0 & 0 \\ 0 & C2_j & 0 & 0 \\ 0 & 0 & C1_j & 0 \\ 0 & 0 & C2_j & -Re \cdot C1_j \end{bmatrix}$$

$$\underline{B} = \begin{bmatrix} B2_j - \phi & 0 & 0 & \pm(k_1)_j Re \\ 0 & B2_j - \phi & 0 & \pm(k_3)_j Re \\ \mp(k_1)_j & \mp(k_3)_j & B1_j & 0 \\ 0 & 0 & B2_j - \phi & -ReB1_j \end{bmatrix} \quad \underline{C} = \begin{bmatrix} A2_j & 0 & 0 & 0 \\ 0 & A2_j & 0 & 0 \\ 0 & 0 & A1_j & 0 \\ 0 & 0 & A2_j & -Re \cdot A1_j \end{bmatrix}$$

and

$$R_1' = 0$$

$$R_2' = Re \left[-\frac{2u_1^n}{\Delta T} + \left(\frac{\partial^2 u_1}{\partial x_1^2} + \frac{\partial^2 u_1}{\partial x_3^2} \right)^n \right] + Re \frac{\partial P^n}{\partial x_1} - 2Re \left(\frac{3}{2} H_1^n - \frac{1}{2} H_1^{n-1} \right) - \frac{\partial^2 u_1^n}{\partial x_2^2}$$

$$R_3' = Re \left[-\frac{2u_2^n}{\Delta T} + \left(\frac{\partial^2 u_2}{\partial x_1^2} + \frac{\partial^2 u_2}{\partial x_3^2} \right)^n \right] + Re \frac{\partial P^n}{\partial x_2} - 2Re \left(\frac{3}{2} H_1^n - \frac{1}{2} H_2^{n-1} \right) - \frac{\partial^2 u_2^n}{\partial x_2^2}$$

$$R_4' = Re \left[-\frac{2u_3^n}{\Delta T} + \left(\frac{\partial^2 u_3}{\partial x_1^2} + \frac{\partial^2 u_3}{\partial x_3^2} \right)^n \right] + Re \frac{\partial P^n}{\partial x_3} - 2Re \left(\frac{3}{2} H_3^n - \frac{1}{2} H_3^{n-1} \right) - \frac{\partial^2 u_3^n}{\partial x_2^2}$$

also,

$$\phi \equiv \left[\frac{2Re}{\Delta T} + \left(k_1^2 + k_3^2 \right)_j \right]$$

$$H_i = -u_\ell \left(\frac{\partial u_i}{\partial x_i} - \frac{\partial u_\ell}{\partial x_i} \right) \qquad \text{(no summation over } i\text{)}$$

and,

$$R_j = \hat{R}'_j$$

Coefficients of the finite-difference operators that appear in the matrices $\underline{A}$, $\underline{B}$, and $\underline{C}$ are given as

$$C2_j = 2/\Delta_{j+1}(\Delta_{j+1} + \Delta_j), \quad B2_j = -2/\Delta_{j+1}\Delta_j, \quad A2_j = 2/\Delta_j(\Delta_{j+1} + \Delta_j)$$

$$C1_j = A1_j = 1/(\Delta_{j+1} - \Delta_j)$$

$$\Delta_{j+1} = (x_2)_{j+1} - (x_2)_j$$

Since all the flow variables in the solution vector contain an imaginary and a real part, the block-inversion process is applied twice for each pair of k_1 and k_3, which are the wavenumbers along x_1 and x_3, respectively.

The assumption of periodicity in x_1 and x_3 eliminates the necessity of applying explicit boundary conditions along these directions. However, due to the presence of solid boundaries along the x_2-direction, no-slip boundary conditions are imposed on u_1, u_2, and u_3 and the pressure at the wall is calculated by a second order approximation from the interior of the flow field. That the pressure boundary conditions are consistent with the x_2-momentum equation at the wall, has been shown by Moin et al. (1978).

Initial conditions were prescribed from the two- and three-dimensional eigensolutions of the Orr-Sommerfeld equation by considering that even for subcritical Reynolds numbers, plane channel flow can be driven to instability if the least stable two-dimensional finite-amplitude Orr-Sommerfeld eigenmodes are interacted with finite-amplitude three-dimensional eigenmodes (Orszag & Kells 1981). The most explosive situation arises when the three-dimensional eigenmodes are aligned with the main flow direction at ±45 to ±60 degrees. Accordingly, we have used the following initial condition

$$\underset{\sim}{u}(\underset{\sim}{x}) = U(x_2,0,0) + u_{2D}(x_2)e^{i\alpha x_1} + u_{3D}(x_2)e^{i\alpha x_1 \pm i\beta x_3} \qquad (8)$$

Here, $U(x_2,0,0)$ is the parabolic velocity profile of plane channel flow. The eigenfunctions $u_{2D}(x2)$ and $u_{3D}(x2)$ correspond to two-dimensional and three-dimensional solutions of the Orr-Sommerfeld equation at Re = 7500, respectively. The two-dimensional solution was obtained for $\alpha = 1$ whereas, the three-dimensional solution was obtained for $\alpha = 1$; $\beta = \pm 1$. A computer program, which essentially uses the Kaplan filtering technique, was used for the solution of the Orr-Sommerfeld equation (Reynolds 1967). The final amplitudes were chosen so that the maximum value of the x_1-directional two-dimensional disturbance was set equal to $0.11U_o$ and the maximum amplitudes of the x_1-directional three-dimensional disturbances were each set equal to $0.05U_o$.

3. RESULTS AND DISCUSSION

The finite-difference system (7) was solved on the CYBER-203 vector processor at NASA/Langley Research Center. A 32×33×32 mesh was employed along the x_1-, x_2-, and x_3-directions, respectively. The computer code was fully vectorized and vectorized library subroutines were used for the main computational operations that the solution technique employs. These vector operations mainly are one-dimensional fast Fourier transform (FFT) to calculate spatial derivatives with the pseudo-spectral method, two-dimensional FFT to transform the equations into k_1-k_3 wave-number space and block-tridiagonal matrix inversion along x_2. For the FFT operations, typical vector lengths were around 1000, which is an optimal vector length to take full advantage of the vector processor. For the block-tridagonal matrix inversion (which is essentially a scalar operation) a vectorized subroutine that inverts a large number of tridiagonal systems simultaneously, was used. This procedure decreases CPU time significantly by reducing the number of scalar operations required to invert each system separately. The fully vectorized code takes about 5 sec. of CPU time per time step for the 32×33×32 mesh to solve the finite-difference system (7) on a computational box, in which the flow is confined between rigid walls at $x_2 = \pm 1$. Periodicity lengths (box lengths) along x_1 and x_3 were chosen so that the smallest wave numbers allowed in the computational domain were equal to $\alpha = 1$ and $\beta = 1$, respectively, i.e., the box length was set equal to 2π along these directions.

It should be recalled that the time-advancement scheme employed in this work is partly explicit (on the convective terms) and partly implicit (on the diffusion and pressure terms). Although in view of linear stability analysis, implicit methods are unconditionally stable (extrapolation to nonlinear equations is sometime vague), the mixed nature of the present scheme as well as the time-accurate nature of the problem under investigation necessitate adherence to stability bounds of explicit schemes. Therefore, in all the calculations reported here, the convective stability condition (the Courant-Friedrichs-Lewy condition) that requires the Courant number (C.N.) to be always less than one and the diffusive stability condition were obeyed. With $(\Delta x_2)_{min} = 0.00694$ and $0.02 < \Delta T < 0.05$, where ΔT is the non-dimensional time-step, through the course of the calculations to C.N. varied as

$$C.N. \equiv \Delta T \left(\left| \frac{u_1}{\Delta x_1} \right| + \left| \frac{u_2}{\Delta x_2} \right| + \left| \frac{u_3}{\Delta x_3} \right| \right)_{max} < 0.4 \qquad (9)$$

whereas the diffusive stability criterion, D, varied as

$$D \equiv \frac{1}{Re} \left[\frac{\Delta T}{(\Delta x)^2_{min}} \right] < 0.14 \qquad (10)$$

so that the diffusive stability condition which requires $D < 0.5$, was also always satisfied.

In the subsequent parts of this section, results obtained from the numerical integration of the finite-difference system (7) for the evolution of the initial disturbances are compared with the experiments of Nishioka et al. (1981). It should, however, be noted that there are several differences existing between the conditions of this experiment and the present conditions. First, periodic boundary conditions employed in the computation along x_1 and x_3 are not realized in the laboratory where the flow is periodic in time. Second, because of periodicity, the computational flow field evolves in time, not in space as in the laboratory. One justification to the first difference can be advanced on the basis of previous numerical experiments, in which transition simulations of the flat-plate boundary

layer (Orszag 1976) and of the plane channel flow (Fasel et al. 1977) with proper inflow-outflow boundary conditions gave similar results to those simulations where periodic boundary conditions were applied. Therefore, it could be expected that the periodic boundary conditions of the present computations should not introduce any significant consequences for comparisons with the laboratory flow. The assumption of streamwise periodicity which implies the evolution of the flow in time (not in space) enables the most efficient use of available computer resolution by resolving only one wavelength. This assumption can be justified on the grounds that in an advected coordinate frame, the spatial evolution of the laboratory flow is essentially equivalent to temporal growth (Orszag & Kells 1980). A third difference between the experiment and the computation is the Reynolds number. The laboratory flow has a subcritical Reynolds number, Re = 5000, whereas the computation was done at Re = 7500 which is linearly unstable for this flow. This selection of the Reynolds number was due to the necessity of forcing the computations into transition and breakdown with the least amount of computer expenses. It should be noted that in their experiments, Nishioka et al. obtained laminar channel flow up to Reynolds numbers around 9000, and found that wall phenomena which are characteristic of the final stages of transition are independent of Reynolds numbers. Hence, the difference between the Reynolds numbers of the experiment and the computation should not have any important consequences for the qualitative comparisons between the two sets of results.

During the computations, data were stored at approximately every 100 time-steps and results at these instances were compared with those of Nishioka et al. (1981) for the various stages of transition. The set of data obtained from the computation that most closely matches a given stage in the laboratory flow is used for comparison with that stage in the experiment. Hence, comparisons are necessarily of a qualitative nature.

In figure 1, a history of the time-evolution of the flow is given in terms of the maximum amplitude of the two-dimensional primary disturbance, its two-dimensional harmonic and the three-dimensional primary disturbance. The trends displayed by these quantities are generally similar to the results of Orszag & Kells (1980) which they obtained from computations per-

formed at Re = 1250. The main features of these trends are the rapid decrease in the two-dimensional primary-wave amplitude and the rapid increase of the amplitude of its harmonic. Also, the three-dimensional primary-wave amplitude first increases, then decreases at around T = 40. In the present calculations, fluctuating variations of the amplitudes are observed to set in as early as T = 18 but, even at later times, the fluctuations are more controlled than those indicated by the results of Orszag & Kells (1980). That no "explosive" instabilities were found in the present computations is in accord with the findings of Nishioka, Asai & Tida (1980), which implies that breakdown in channel flow is as gradual as the growth of instabilities found in free shear flows.

Plane-averaged (over the $x_1 - x_3$ plane) flow-field quantities which are representative of various stages of transition are shown in figures 2-7. Plots of plane-averaged (mean) velocity profiles, u_1, are shown in figure 2 for laminar (initial), late transition and "early-turbulence" stages at T = 0, T = 42 and T = 50, respectively. The u_1 distribution at T = 50 has a strong resemblance to the turbulent channel flow profile, with increased velocity gradient at the wall and with a full profile indicative of turbulent mixing. Although, as expected, $\langle u_1 \rangle$ profiles do not show any fluctuations (or inflexions), plots of instantaneous velocity profiles do show very strong inflexions, especially in the regions close to the walls (figure 3). This indicates that the interaction of two- and three-dimensional waves close to the walls is the central mechanism that drives the flow to instability. This is in accord with the idea that the flow will undergo transition only for a selected band of spanwise wavenumbers, the most "dangerous" of which result in three-dimensional disturbances with maxima occurring close to the walls (Orszag & Kells 1980). In figure 4, the velocity profile $\langle u^+ \rangle = \langle u_1 \rangle / u_2$ versus $y^+ = x_2 u_2 / \nu$ is plotted; here u_2 is the friction velocity and is calculated from $d \langle u_1 \rangle / dx_2$ at the wall. Although the plots indicate the formation of a sublayer, and the change from T = 42 to T = 50 shows a gradual approach to the law-of-the-wall, the difference is still especially apparent in the logarithmic region. The values obtained from figure 8 of Nishioka et al. (1981) provides a fairly good comparison with the computation at T = 42; in fact, computational results at T = 42 will be presented as representing the five-spike stage of the experiment. At

At T = 42, the Reynolds number based on the friction velocity is equal to 196 and, as expected, is considerably larger than its initial (laminar) value of 122.

Plots of plane-averaged fluctuation intensities, $\langle (u_1 - \langle u_1 \rangle)^2 \rangle$, are shown in figure 5 at various T. There are several interesting features of this figure. Firstly, at T = 12, the shift in the position of peak amplitude towards the channel center ($x_2 = 0.4$), as well as the increase in the maximum amplitude, indicate that the computation is developing in a manner compatible with the experimental observations pertaining to this stage of the transition process (Tani 1969). In addition to this, it will be shown later that there is a substantial increase in the spanwise vorticity, ω_z, away from the wall at around $x_2 = 0.4$. Secondly, in accordance with the laboratory flow of Nishioka et al. (1981) at later stages in computation (e.g. at T = 42), the intensity profiles display a second peak occurring close to the wall which should be associated with turbulence production. However, in spite of these similarities, a comparison of the computational results at T = 42 and the five-spike stage of the experiment (Nishioka et al.) shows that the locations of the peak positions do not coincide and the peak value obtained in the experiment is about 15 percent greater than that obtained from the computation.

Spanwise variations of u_1 and u_3 at T = 42 are plotted at various distances along x_2 in figures 6 and 7, respectively. These figures indicate that at this stage the flow is highly three-dimensional; however, the spanwise symmetry imposed by the initial conditions is still retained. An estimate of the flow field resolution along x_3 can be obtained from the spanwise distance between peak position, λ. Nondimensionalized by u_2 and ν typically $\lambda = 120$. This is larger than but comparable to $\lambda = 80$, which is the typical spanwise length in the laboratory flow during the five-spike stage (Nishioka et al. 1981). It should be noted that the spanwise characteristic length in wall turbulence is about 100. It could, therefore, be asserted that, at this stage present results are representative of initial wall turbulence.

A more detailed description of the transition process can be obtained from contour plots of equi-shear lines, $\frac{\partial u_1}{\partial x_2}$ (which correspond to approximate

spanwise vorticity, ω_z) in the $x_1 - x_2$ plane at the position of maximum u_1/U_o. Computational results that correspond to the various stages of the laboratory flow are presented in figures 8-12. In figures 9a - 11a, figures 4-6 of Nishioka et al. (1981) are also presented for comparison with the present computations. In figure 8, contour plots corresponding to the initial conditions and in figure 9, contour plots corresponding to the "one spike" stage (T = 0 and T = 12, respectively) are shown. In both the laboratory flow and the computation, the typical head of the shear layer appears very clearly at the one-spike stage, indicating the formation of a shear layer away from the wall at about $x_2 = 0.4$ due to the induced velocity from the streamwise vortex system. In the experiment, the sudden dip of the shear layer from the high-velocity outer flow to the low velocity region appears as a kink. This is not very clear in the computation and can be attributed to inadequate resolution along x_2 in the outer portions (close to the centerline) of the flow field. Inadequate mesh spacing in these portions of the flow field away from the wall manifests itself in the comparison of contour levels and concentrations of approximate spanwise vorticity inside the "head" of the shear layer. This comparison mainly reveals that the laboratory flow exhibits higher vorticity levels than are indicated by the computation. However, since the mesh is finely clustered along x_2 close to the wall, vorticity concentrations in this region are adequately resolved by the numerical simulation.

Figure 10 shows equi-shear lines at T = 22 corresponding to the three-spike stage of the laboratory flow. In both the experiment and the computation, due to the secondary instability manifested in the previous stage, breakdown of flow structures into smaller scales are observed. In the experiment, the growth of the kinked portions of the equi-shear lines into the so-called "hairpin eddies" is clearly depicted. The computation displays a similar evolution, with the head of the shear layer lifted up towards the channel centerline, and the kink in the shear layer being quite apparent in this stage of the computation. Simultaneously with this activity taking place in the outer (high speed) portions of the flow field, both the experiment and the computation show an intense shear layer developing close to the wall, which is indicative of turbulence generation. Although it is generally agreed that hairpin eddies which are lifted towards the centerline erupt into turbulent spots, it seems likely that wall-turbulence

is also closely associated with vorticity dynamics that take place simultaneously with the eruption of hairpin eddies. Contours of equi-shear lines at T = 42 corresponding to the five-spike stage of the experiment are shown in figure 11. The intense shear-layer developed in the wall region is apparent in both the experiment and the computation. Vorticity levels in the laboratory flow and the computation are comparable but the laboratory flow indicates generally higher levels. The most significant feature in figure 11 is the existence of distinct vortex structures in the wall region both in the laboratory flow and in the computation. These vortices are aligned close to 45° to the mean flow direction and show a close resemblance to the energetic horseshoe vortices which are characteristic of wall-turbulence. It is these vortices (turbulent eddies) that are mainly responsible for extracting energy from the mean shear (Tennekes & Lumley 1974, p. 41). In figure 12, equi-shear lines are shown at T = 50. Here, all high-shear concentration and intense vorticity dynamics are confined to the wall region. Also, ow field is characterized by scales which are much smaller than those observed in the earlier stages, somewhat indicating that the flow field at this stage assumes a turbulent-like character.

Contours of streamwise vorticity, ω_x, are shown in figures 13-17 at various instances in time in the x2 - x3 plane at the position of maximum u_1/U_o. Figure 13 displays that at T = 0, the counter-rotating vortex system which is due to the prescribed initial conditions is relatively weak and there are no vorticity concentrations close to the wall. Figure 14 shows ω_x at T = 12, corresponding to the one-spike stage of the laboratory flow. At this stage in the simulation, the initial counter-rotating vortex system is still evident and there is an enhancement and concentration of streamwise vorticity close to the wall. Streamwise vorticity contours corresponding to the three-spike stage of the laboratory flow are shown in figures 15 at T = 22, where ω_x is enhanced and its magnitude is comparable to the lateral component, ω_z. In addition to this enhancement of ω_x, figure 15 displays occurrence of patches of vorticity of scales much smaller than the initial counter-rotating vortices. Formation of alternating positive (solid lines) and negative (dashed lines) vorticity regions close to the wall is also evident from this figure. Figure 16 and 17 show contours of streamwise vorticity during the multi-spike and early-turbulence

stages, i.e. at T = 42 and T = 50, respectively. In these figures, the major features are further enhancement of streamwise vorticity, breakdown into smaller scales and concentration of streamwise vorticity close to the walls. Details of ω_x contours in the vicinity of the wall are shown in figure 18 at T = 50 where the region between the lower wall (x2 = -1.0) and x_2 = -0.92 is magnified. The most interesting aspect of this figure is the distinct pattern of alternating regions of very high concentrations of positive and very high concentrations of negative vorticity; however, due to magnification contour lines are distorted in this figure. The alternating streamwise-vorticity region is usually associated with an induced velocity field that is responsible for vorticity production during the final stages of the transition process (Komoda 1967). It should also be noted that the alternating structure of positive and negative concentrations of vorticity close to the wall is a very distinct feature of fully developed wall-turbulence (Moin & Kim 1981).

The mechanism that is responsible for the generation of vorticity concentrations is usually explained as vortex stretching (and deformation) by the mean flow. The stretching and deformation moves downstream with a translation velocity that induces lower local mean velocity of the upstream edge of the vorticity layer than its downstream edge (Komoda 1967). An examination of contours of mean velocity (figure 19) along with the spanwise vorticity contours at T = 22 (figure 10) in the $x_1 - x_2$ plane at the position of maximum u_1/U_o clearly shows a similar trend. The nose of the negative streamwise vorticity layer (which corresponds approximately to regions with high concentrations of equi-shear lines) is generally associated with higher velocities than the upstream region and large variations of the local mean velocity exist within the layer.

Normal velocity, u_2, contours are shown in figures 21-24 during the three-spike, multi-spike and early-turbulence stages at the position of maximum u_1/U_o. Figure 20 shows u_2-contours in the $x_1 - x_2$ plane at T = 22, corresponding to the three-spike stage of the laboratory flow. In this figure, there is clear evidence of the beginning of an alternating up- and -down flow similar to the pattern described by Kovasznay et al. (1967), which is characterized by the intense updrift accompanied by fluid drifting

down at both sides. This alternating structure of up-and-down flow in the $x_1 - x_2$ plane is more evident at T = 42 (figure 21), corresponding to the multi-spike stage of the experiment. Also in this figure, alternating regions of fluid with scales much smaller than those at T = 22, are clearly depicted. In figure 22 and 23, normal velocity contours are shown in the $x_2 - x_3$ plane at T = 42 and T = 50 corresponding to the multi-spike and early-turbulence stages, respectively. These contours are plotted in the region between the lower wall ($x_2 = -1.0$) and $x_2 = -0.92$. In these figures, the development of the up-and-down pattern of the fluid close to the wall is observed; the contours at T = 50 display alternating structures very similar to the characteristic streak-like structures found in the wall region of turbulent channel flow (Moin & Kim 1981).

4. SUMMARY AND CONCLUDING REMARKS

In this study, final stages of transition to turbulence in plane channel flow have been simulated by a direct numerical solution of the Navier-Stokes equations. Results were compared with the experiments of Nishioka et al. (1981) and it was found that, in spite of the limited resolution of the 32×33×32 grid employed in the computations, the simulation was capable of reproducing most of the essential features of wall phenomena observed in the laboratory flow. Grid resolution in the x_1- and x_3-directions, along which the flow is periodic, was found to be adequate to capture the sequence of events that lead to early turbulence. Vorticity and velocity contours in the vicinity of the lower wall indicated formation of horseshoe vortices and, at later stages, streak-like structures alternating in the spanwise direction. Typically, the spanwise characteristic length, λ, inferred from the spanwise variations of u_1 and u_3, was found to be around $\lambda = 120$, which is close to $\lambda = 100$ of fully developed wall turbulence. In agreement with the experiment, it was found that during the later stages of transition, flow field statistics indicate the formation of a laminar sublayer; however, the development of the logarithmic region and hence the approach to fully developed turbulence is slow.

The main deficiency of this study inevitably stems from limited spatial resolution and manifests itself in several ways. Firstly, at later stages

of the computation, e.g. for T = 42, the computation was not able to maintain the total disturbance energy (turbulent kinetic energy). This is not surprising and can be explained on the grounds that close to the wall, the available mesh is not able to resolve the characteristic large-scale structures, which appear as finely spaced streaks. Insufficient mesh resolution could also result in lower gradients of the mean velocity in the viscous sublayer. The combined effect of these is less turbulence production and therefore indefinitely decaying turbulent kinetic energy. Secondly, the finite cut-off wave numbers along x_1 and x_3 prevent energy transfer down the wave-number space. Accordingly, at large T, pollution of Fourier modes and accumulation of excess energy at low wave numbers become very significant sources of inaccuracy. Hence, proper simulation of transition beyond the early turbulence stage necessitates the use of the higher grid resolution and even then, the incorporation of subgrid scale turbulence modeling for an accurate and realistic representation of the flow field phenomena.

This work was supported by NASA/Langley Research Center under Grant No. NAG-1-228. The author is indebted to P. Moin, J.H. Ferziger, and W.C. Reynolds for helpful discussion and to P.J. Bobbitt and W.D. Harvey for their interest and encouragement during the course of this work.

REFERENCES

Fasel, H.; Bestek; H., and Schefenacker, R.: Numerical simulation studies of transition phenomena in incompressible, two-dimensional flows. Proc. Laminar-Turbulent Transition, AGARD Conf., No. 224, 1977, p. 14-1.

George, W.D.; and Hellums, J.D.: Hydrodynamic stability in plane Poiseuille flow with finite-amplitude disturbances. J. Fluid Mech. 78, 355, 1972.

Kao, T.W; and Park, C.: Experimental investigations of the stability of channel flows. Part 1. Flow of a single liquid in a rectangular channel. J. Fluid Mech. 43, 145, 1970.

Klebanoff, P.S.; Tidstrom, K.D.; and Sargent, L.M.: The three-dimensional nature of boundary-layer instability. J. Fluid Mech. 12, 1, 1962.

Kleiser, L.: Spectral simulations of laminar-turbulent transition in plane Poiseuille flow and comparison with experiments. Proc. 8th Int. Conf. on Numerical Methods in Fluid Dynamics, Aachen, 1982.

Komoda, H.: Nonlinear development of disturbance in a laminar boundary layer. Phys. Fluids. 10, Suppl., 87, 1967.

Kovasznay, L.S.G.; Komoda, H.; and Vasudeva, B.R.: Detailed flow field in transition. Proc. Heat Transfer and Fluid Mechanics Institute, 1962, p.1.

Mansour, N.N.; Ferziger, J.H; and Reynolds, W.C.: Large eddy simulation of turbulent mixing layer. Dept. Mech. Engng. Stanford Univ. Rep. TF-11, 1978.

Moin, P.; and Kim, J.: Numerical investigation of turbulent channel flow. NASA TM-81309, 1981.

Moin, P.; Reynolds, W.C.; and Ferziger, J.H.: Large eddy simulation of incompressible turbulent channel flow. Dept. Mech. Engng. Stanford Univ. Rep. TF-12, 1978.

Nishioka, M.; Asai, M.; and Iida, S.: An experimental investigation of the secondary instability. In Laminar-Turbulent Transition (ed. R.E. Meyer), Academic Press, 113, 1981.

Nishioka, M.; Asai, M.; and Iida, S.: Wall phenomena in the final stage of transition to Turbulence. In Transition and Turbulence (ed. R.E. Meyer), Academic Press, 113, 1981.

Orszag, S.A.: Comparison of pseudo spectral and spectral approximation. Studies in Appl. Math., LI, No. 3, 253, 1972.

Orszag, S.A.: Turbulence and transition: A progress report. Proc. 5th Int. Conf. on Numerical Methods in Fluid Dynamics (ed. A.I. Van de Vooren and P.J. Zandbergen), Springer, 32, 1976.

Orszag, S.A.; and Kells, L.C.: Transition to turbulence in plane Poiseuille and plane Couette flow. J. Fluid Mech., 96, 159, 1980.

Orszag, S.A.; and Patera, A.T.: Subcritical transition to turbulence in planar shear flows. Phy. Rev. Let. 45, 989, 1981.

Reynolds, W.C.: A Fortran IV program for solution of the Orr-Sommerfeld equation. Dept. Mech. Engng. Stanford Univ. Rep. FM-4, 1967.

Tani, I.: Boundary layer transition. Ann. Rev. Fluid Mech. 1, 169, 1969.

Tennekes, H.; and Lumley, J.L.: A First Course in Turbulence. MIT Press, 1972.

Theodorsen, T.: The structure of turbulence in 50 Jahre Grenzschichtforschung. Friedr. Vieweg of Sohn, 55, 1955.

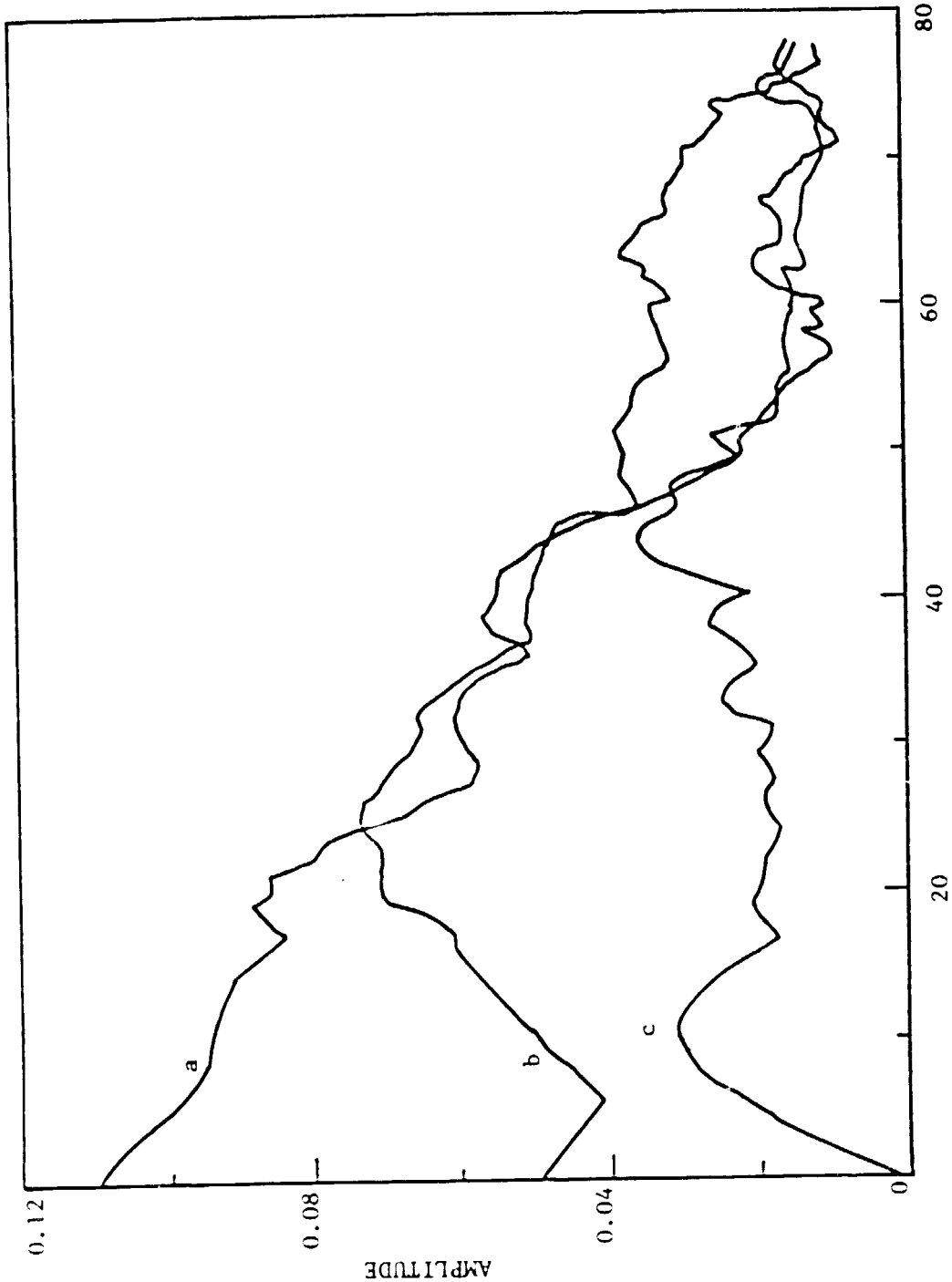

Figure 1. Time-history of maximum disturbance amplitudes. (a) two-dimensional primary; (b) three-dimensional primary; (c) two-dimensional harmonic.

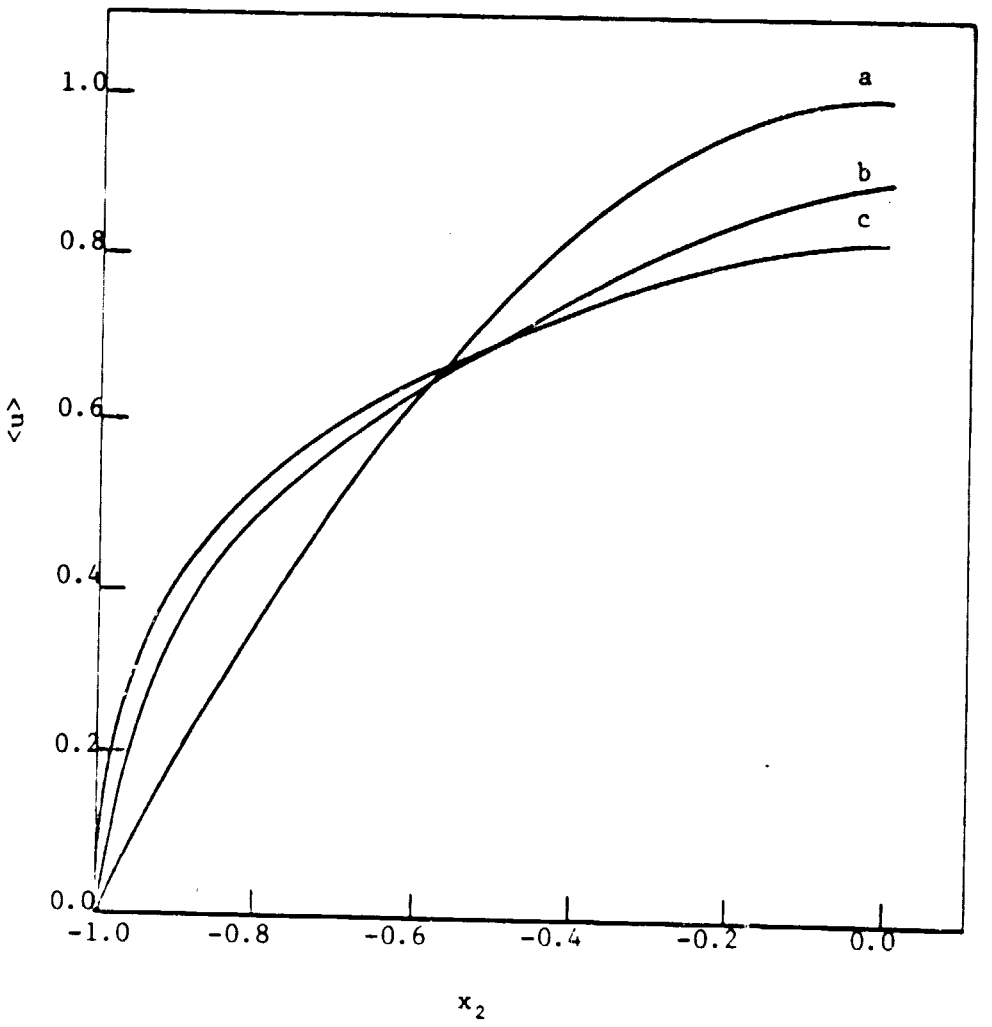

Figure 2. Plots of plane-averaged mean velocity profiles. (a) T = 0; (b) T = 42; (c) T = 50.

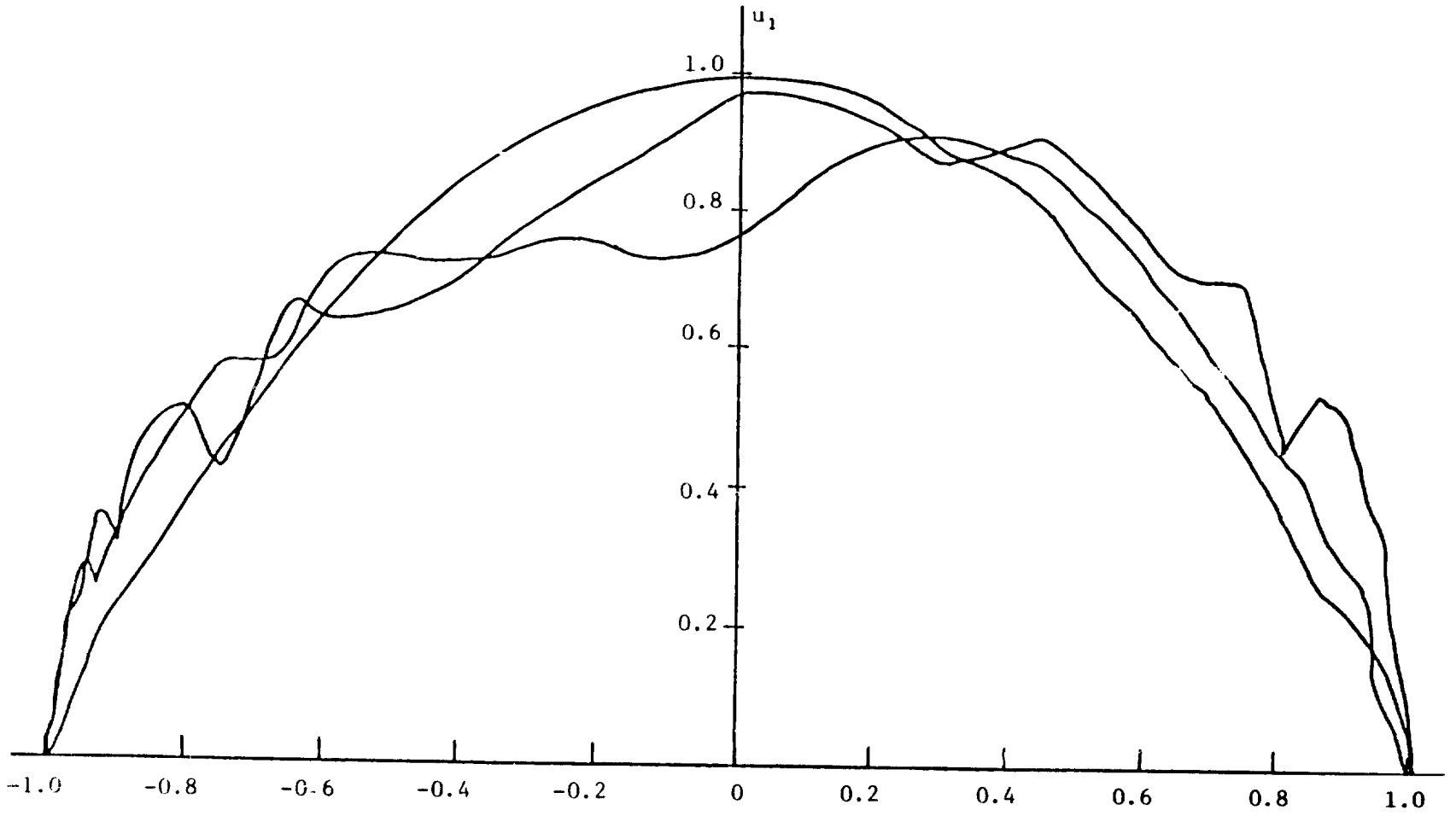

Figure 3. Plots of instantaneous velocity profiles at $x_1 = 3\pi/2$, $x_3 = \pi/2$. (a) T = 12; (b) T = 42; (c) T = 50.

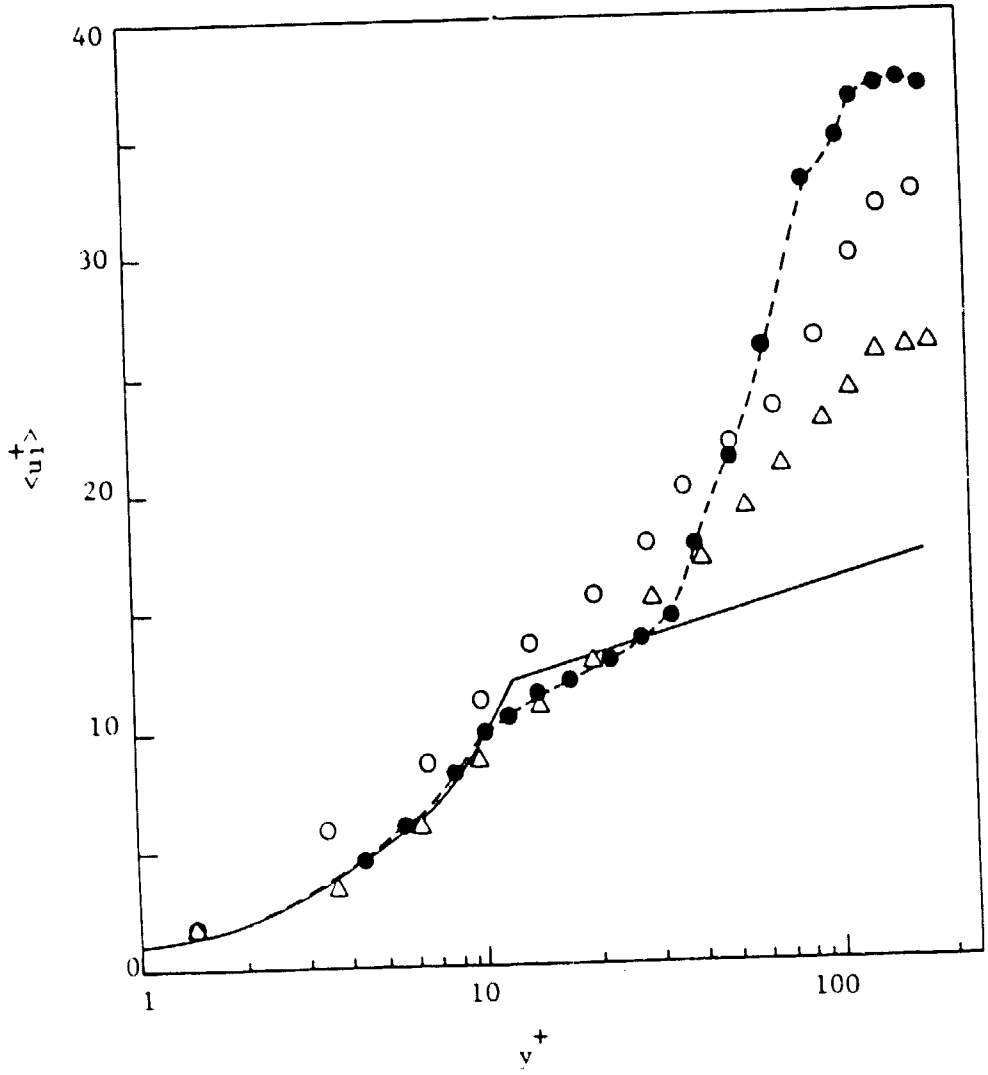

Figure 4. Plots of plane-averaged mean velocity in wall units; o, T = 42; Δ, T = 50; ——, law-of-the-wall; ●--, experiments of Nishioka et al. (1981) at the five-spike stage.

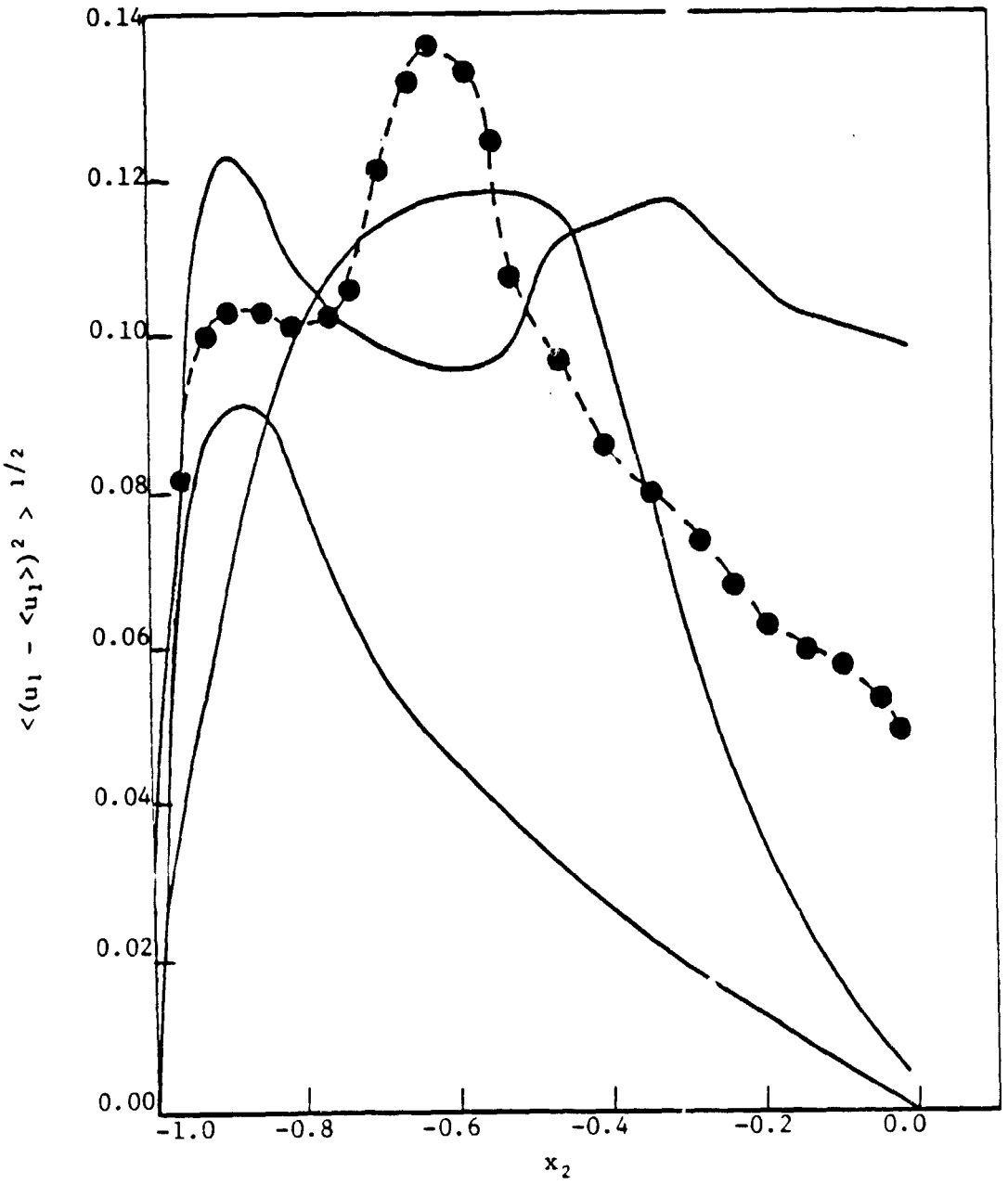

Figure 5. Plots of plane-averaged fluctuating intensities. (a) T = 0; (b) T = 22; (c) T = 42; ●--, experiments of Nishioka et al. (1981) at the five-spike stage.

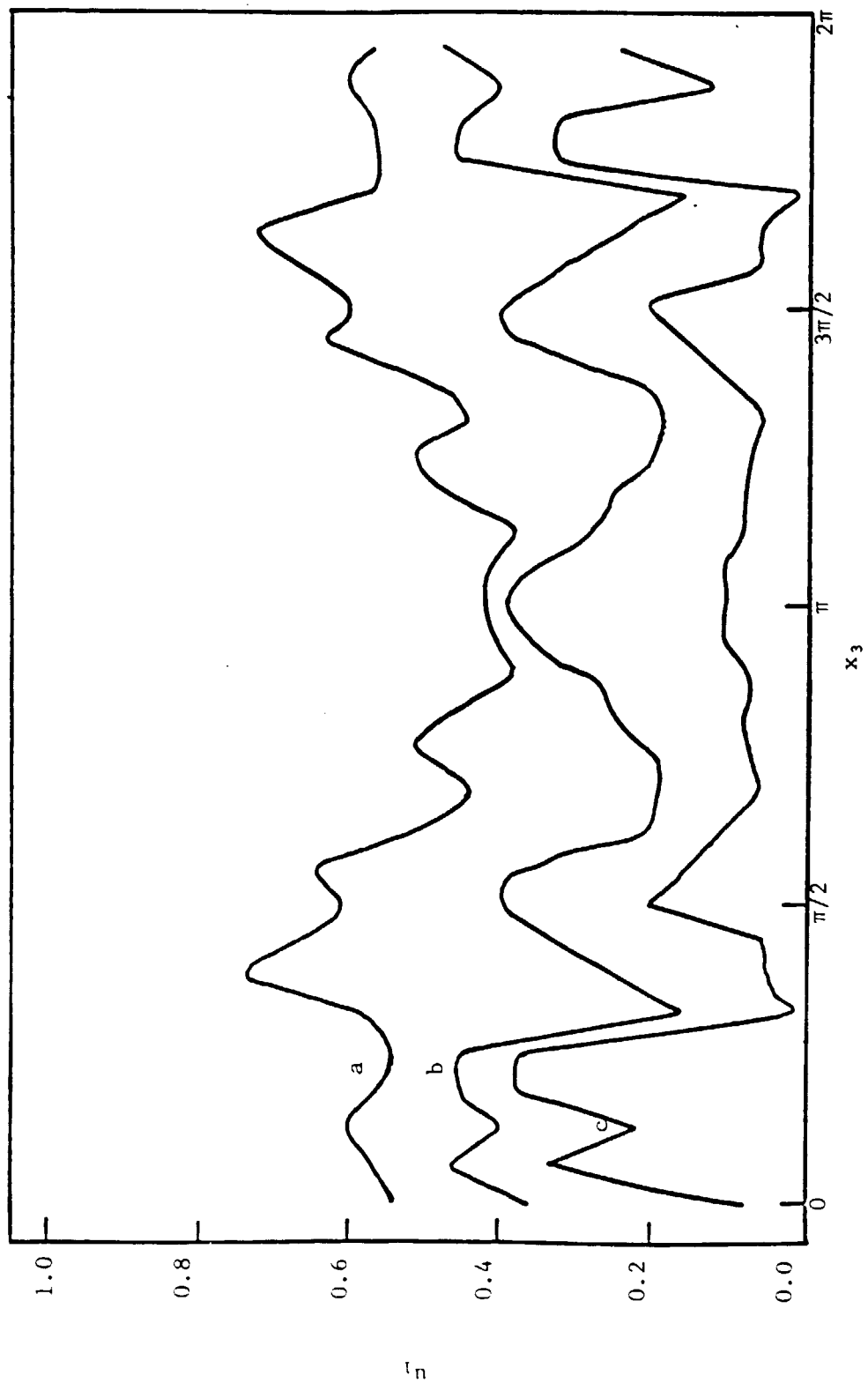

Figure 6. Spanwise variations of u_1 at T = 42. (a) x_2 = 0.029; (b) x_2 = 0.099; (c) x_2 = 0.256.

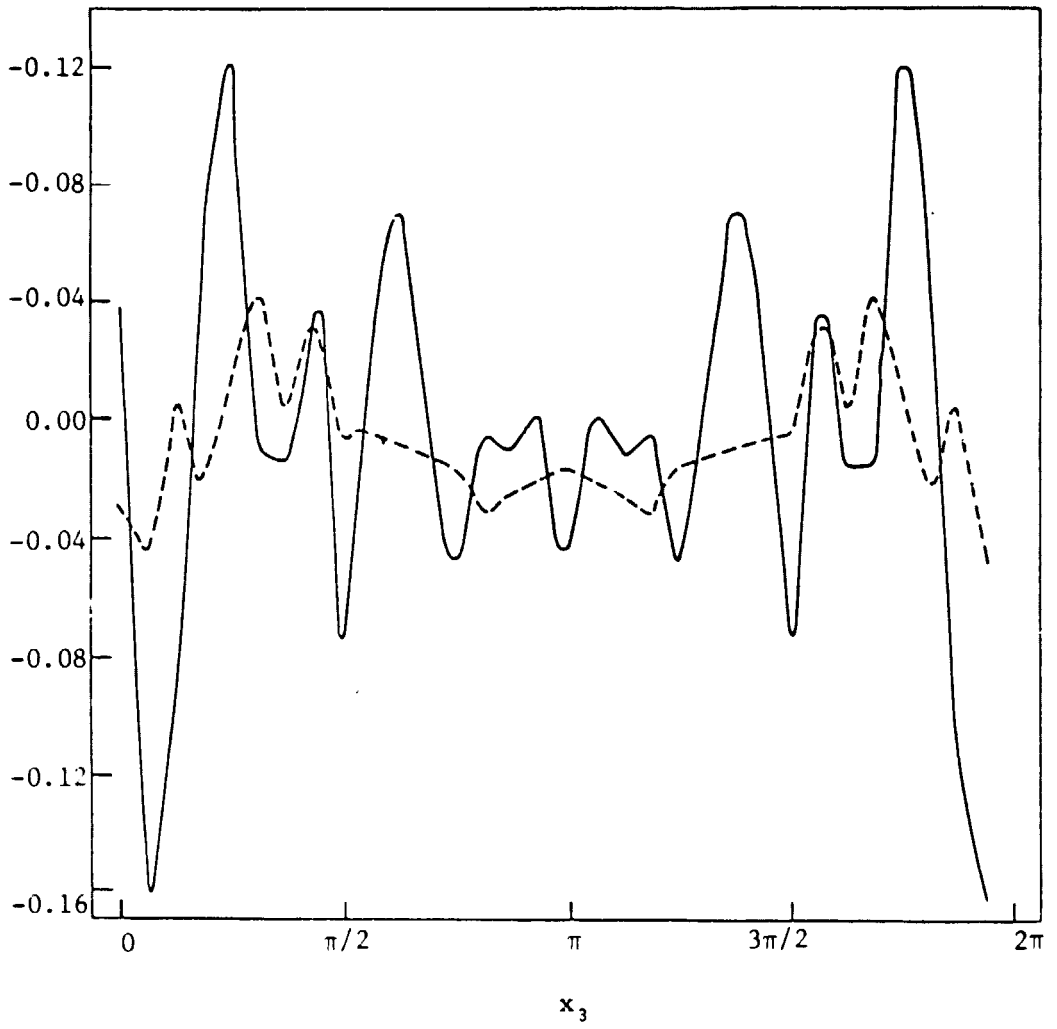

Figure 7. Spanwise variations of u_3 at T = 42. (a) x_2 = 0.029; (b) x_2 = 0.099; (c) x_2 = 0.256.

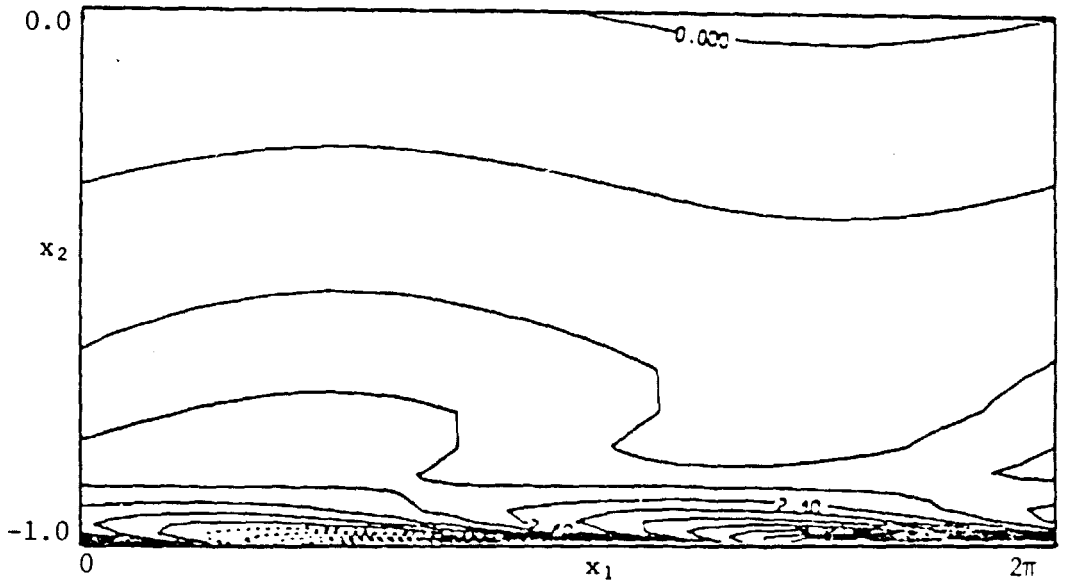

Figure 8. Contour plots of $\frac{\partial u_1}{\partial x_2}$ at T = 0 in the x_1, x_2 plane. Contours from -0.3 to 7.2.

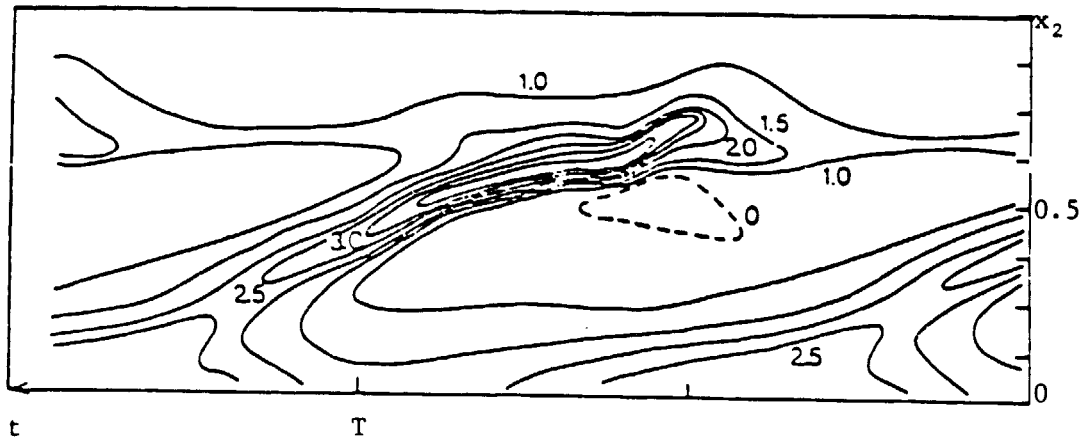

(a)

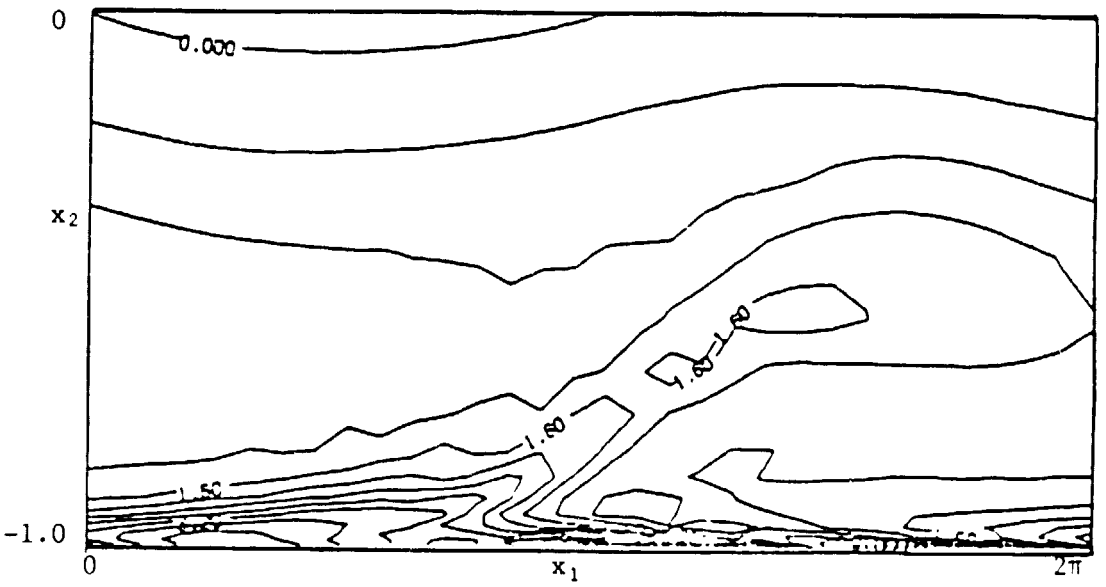

(b)

Figure 9. Contour plots of $\frac{\partial u_1}{\partial x_2}$. (a) three-spike stage, figure from Nishioka et al. (1981); (b) computations at T = 42 in the x_1, x_2 plane; contours from -1.2 to 6.0.

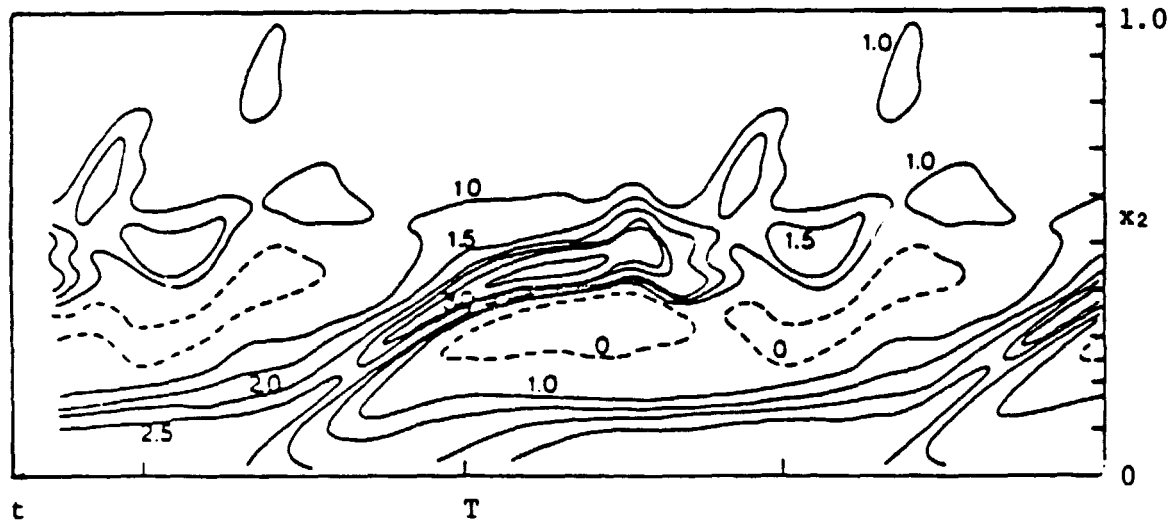

(a)

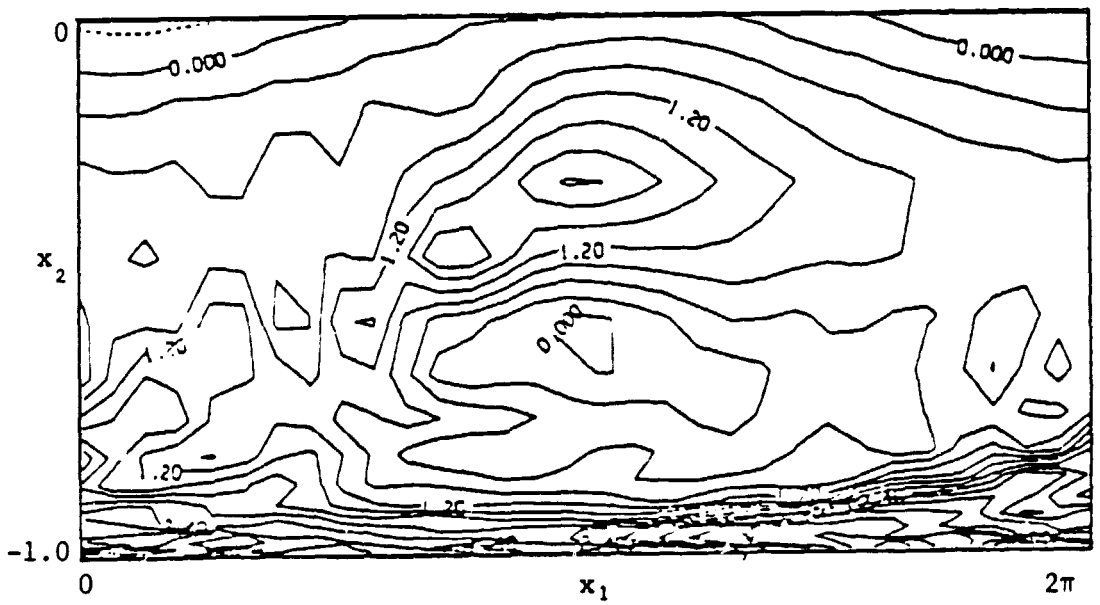

(b)

Figure 10. Contour plots of $-\frac{\partial u_1}{\partial x_2}$. (a) three-spike stage, figure from Nishioka et al. (1981); (b) computations at T = 22 in the x_1, x_2 plane; contours from -0.3 to 5.1.

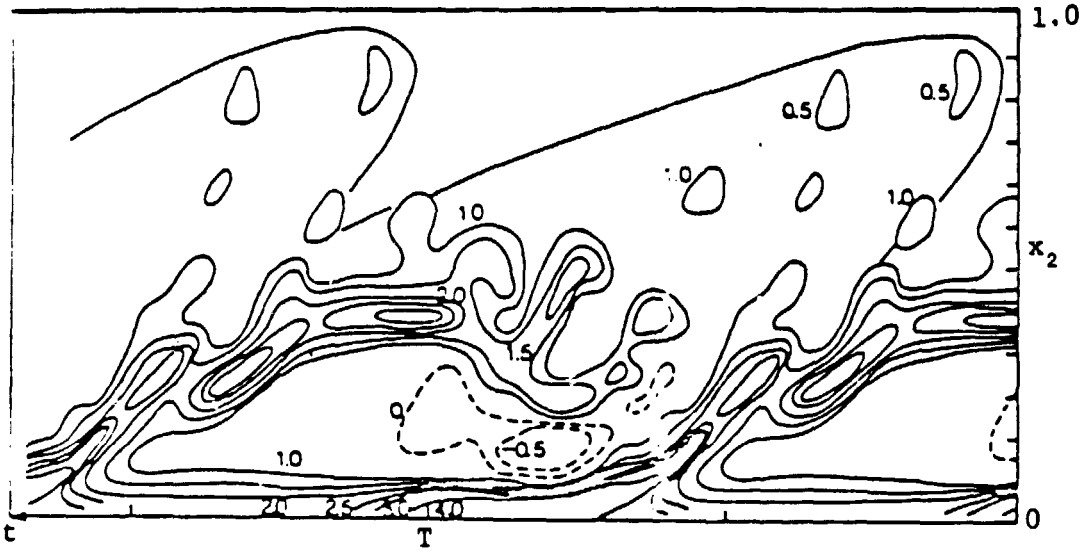

(a)

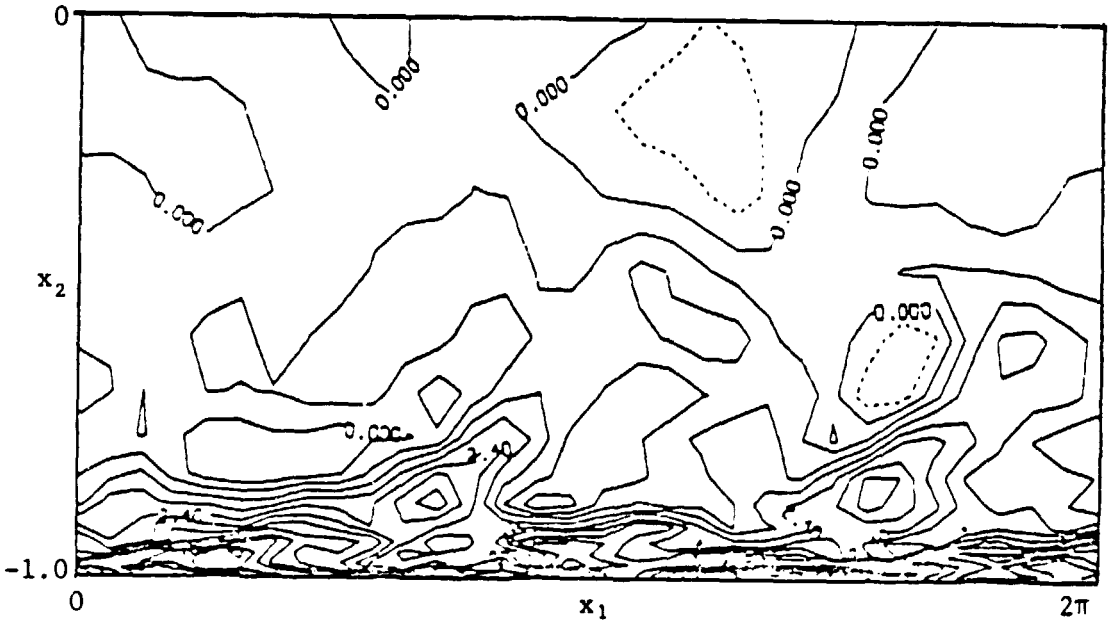

(b)

Figure 11. Contour plots of $\frac{\partial u_1}{\partial x_2}$. (a) three-spike stage, figure from Nishioka et al. (1981); (b) computations at T = 42 in the x_1, x_2 plane; contours from -0.6 to 9.0.

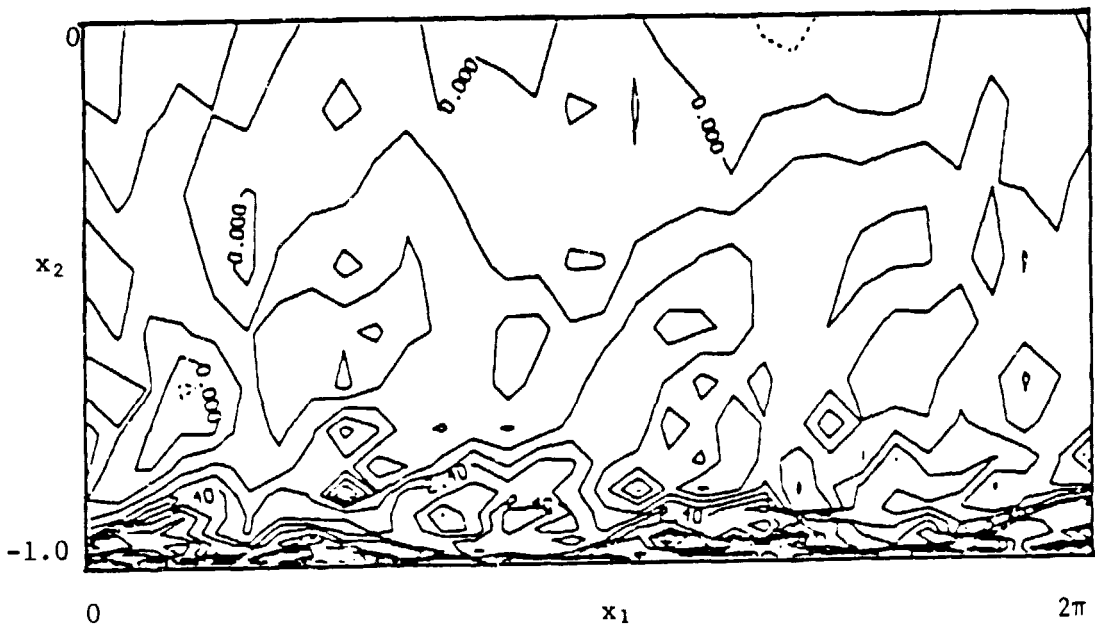

Figure 12. Contour plots of $\frac{\partial u_1}{\partial x_2}$, at T = 50 in the x_1, x_2 plane; contours from -0.6 to 9.0.

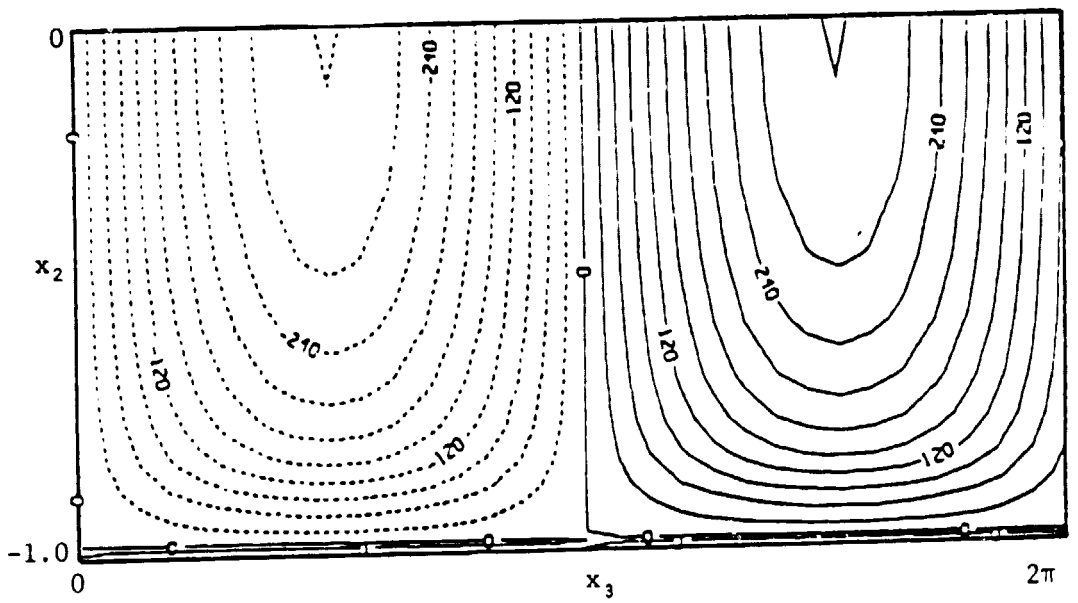

Figure 13. Contour plots of ω_x in the x_2, x_3 plane at T = 0; contours from -0.03 to 0.03, labels scaled by 10000.

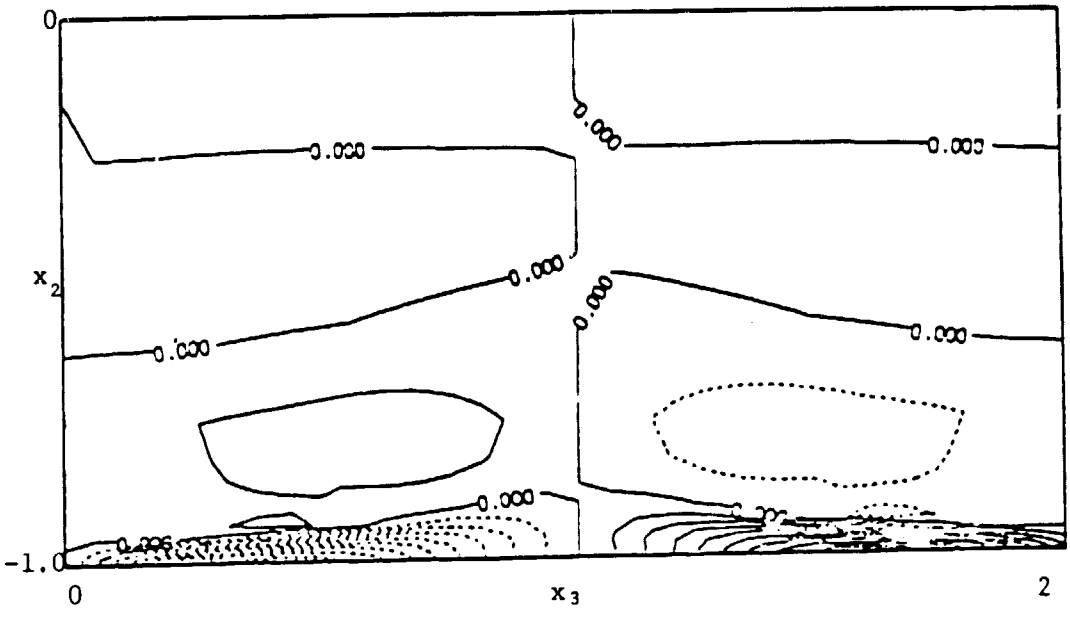

Figure 14. Contour plots of ω_x in the x_2, x_3 plane at T = 12; contours from -1.6 to 1.6.

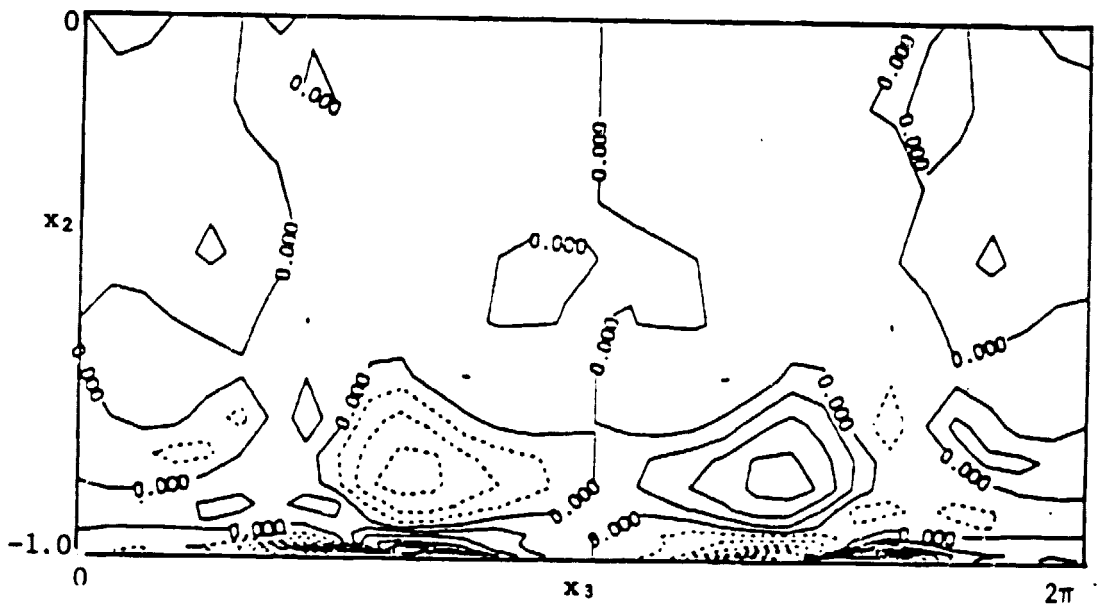

Figure 15. Contour plots of ω_x in the x_2, x_3 plane at T = 22; contours from -4.8 to 4.8.

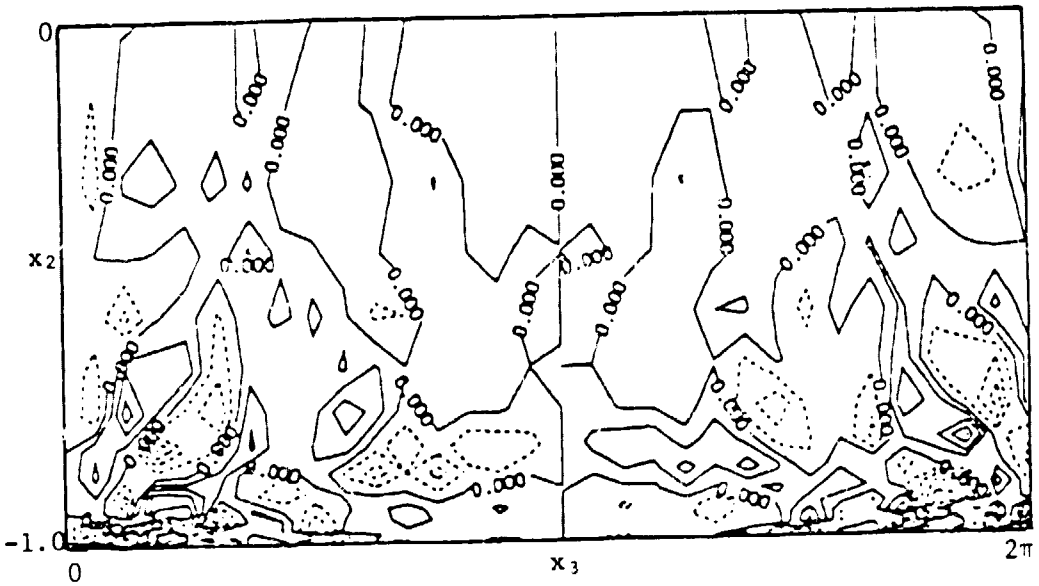

Figure 16. Contour plots of ω_x in the x_2, x_3 plane at T = 42; contours from -6.4 to 6.4.

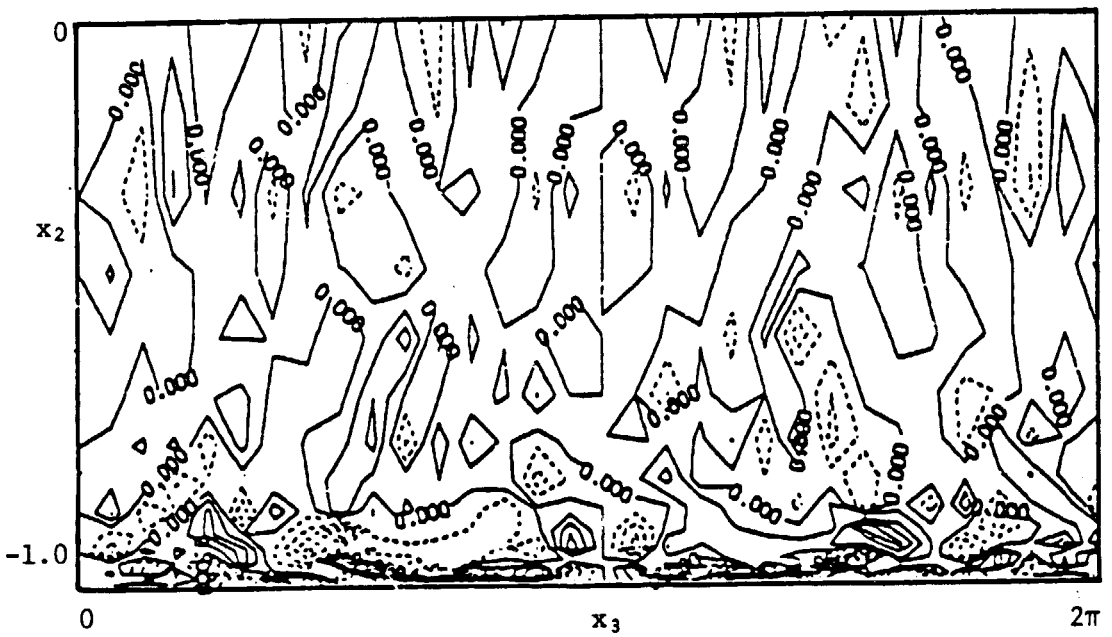

Figure 17. Contour plots of ω_x in the x_2, x_3 plane at T = 50; contours from -5.4 to 5.4.

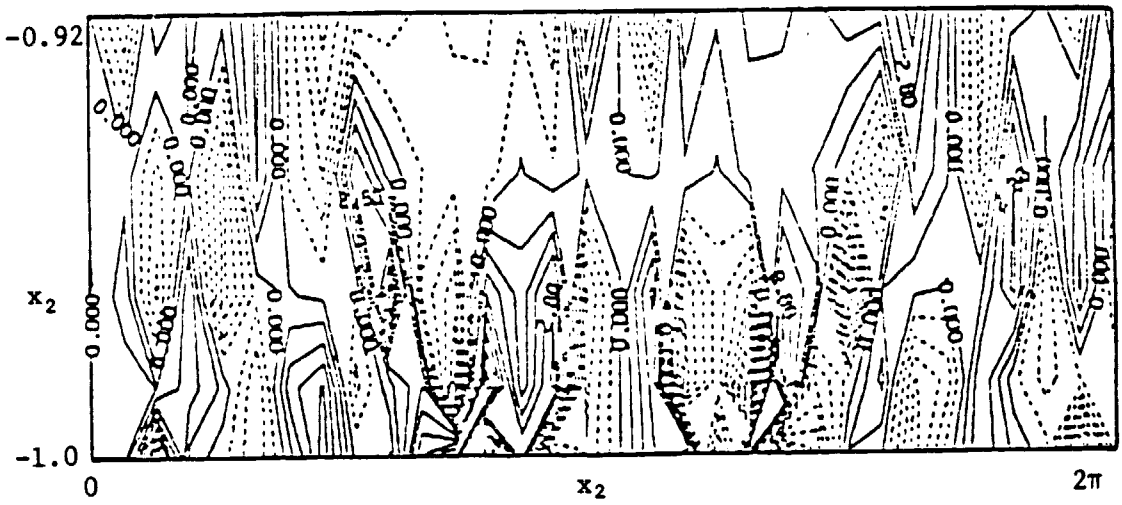

Figure 18. Contour plots of ω_x in the x_2, x_3 plane at T = 50; contours from -5.6 to 5.6.

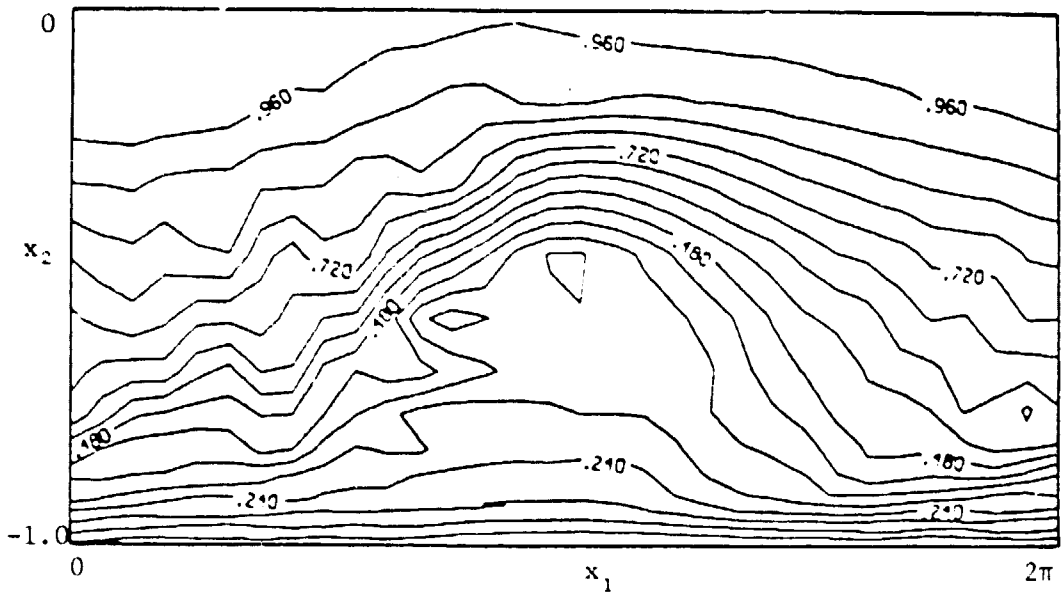

Figure 19. Contour plots of u_1 in the x_1, x_2 plane at T = 22; contours from -0. to 0.96.

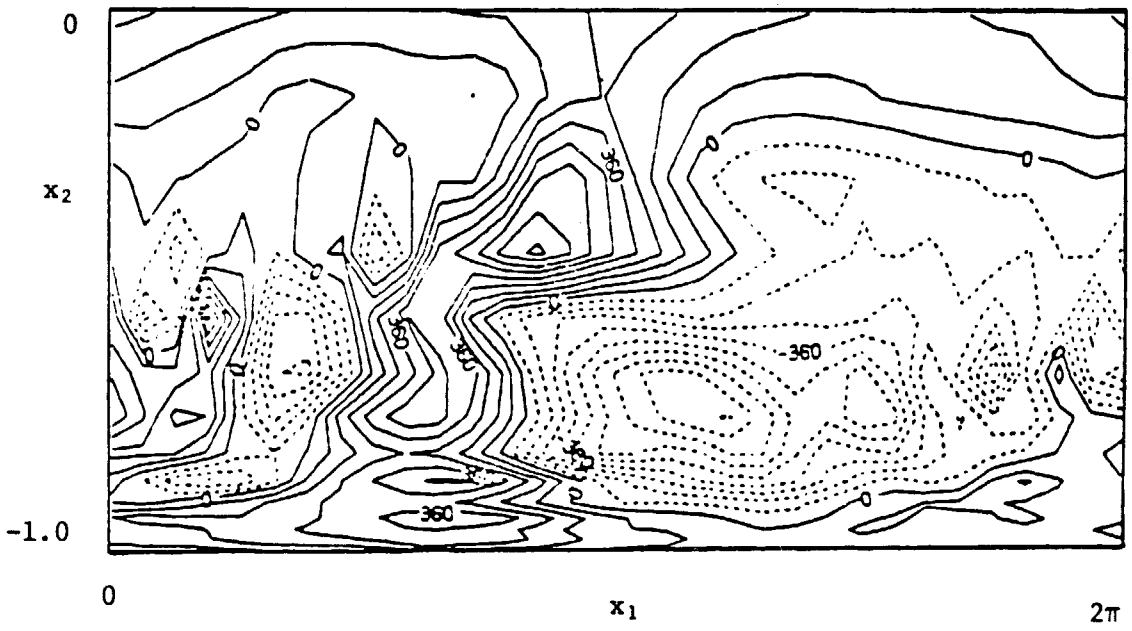

Figure 20. Contour plots of u_2 in the x_1, x_2 plane at T = 22; contours from -0.081 to 0.072 labels scaled by 1000.

ORIGINAL PAGE IS
OF POOR QUALITY

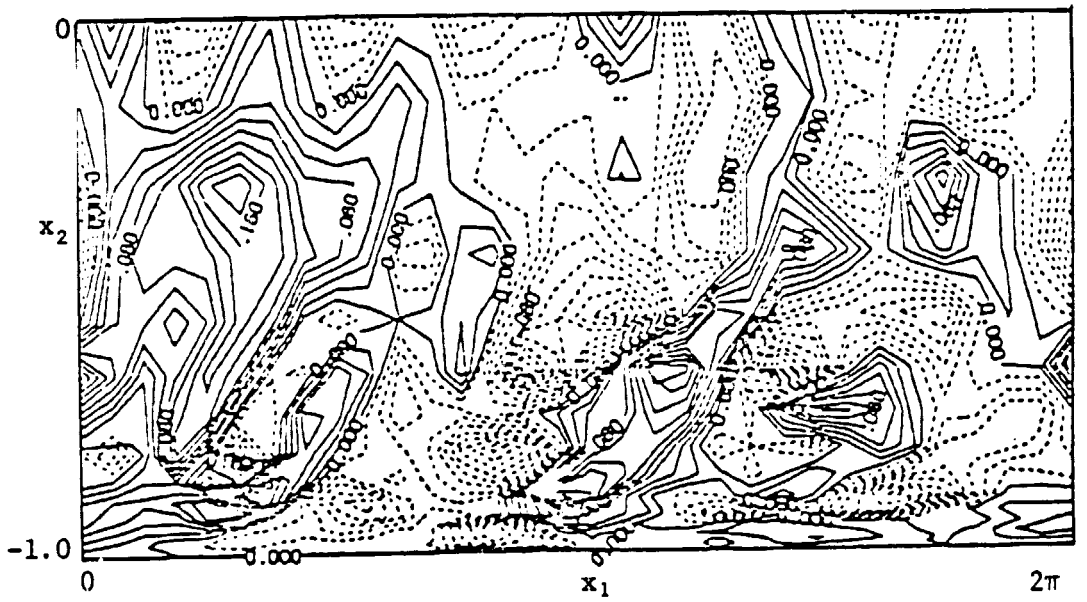

Figure 21. Contour plots of u_2 in the x_1, x_2 plane at T = 42; contours from -0.22 to 0.20.

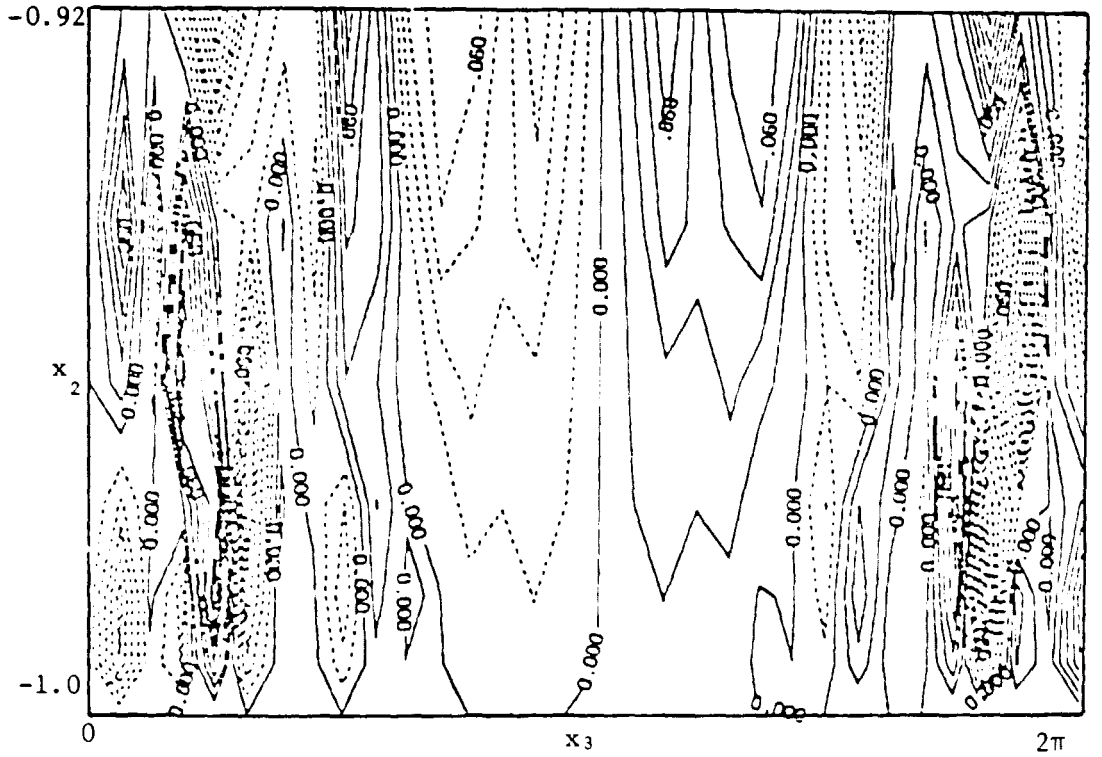

Figure 22. Contour plots of u_2 in the x_2, x_3 plane at T = 42 in the vicinity of the lower wall; contours from -0.135 to 0.135.

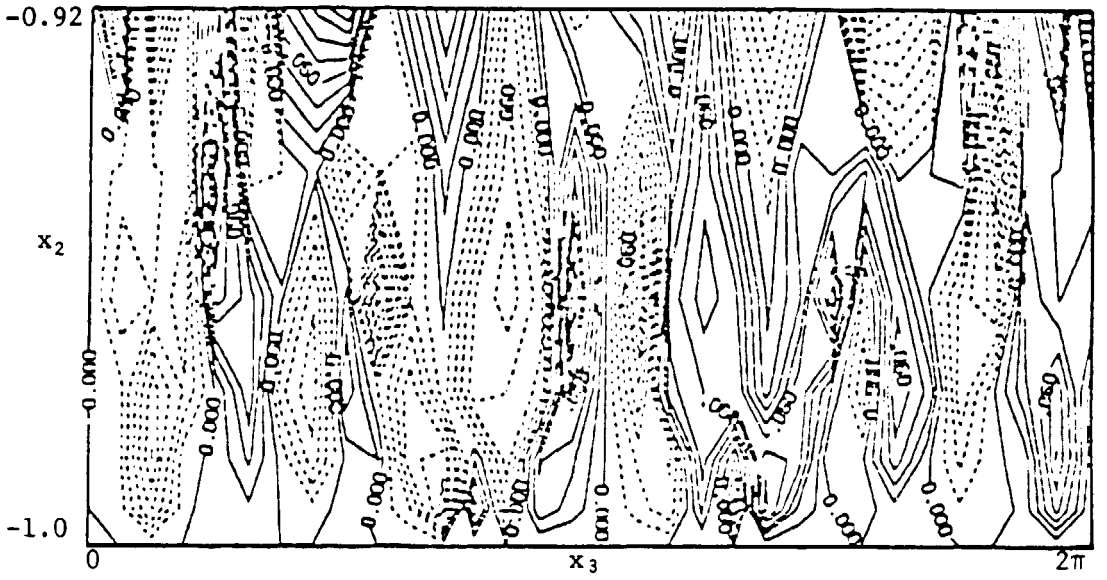

Figure 23. Contour plots of u_2 in the x_2, x_3 plane at T = 50 in th vicinity of the lower wall; contours from -0.135 to 0.135.